

Degradation-Aware Residual-Conditioned Optimal Transport for Unified Image Restoration

Xiaole Tang, Xiang Gu, Xiaoyi He, Xin Hu, Jian Sun

Abstract—Unified, or more formally, all-in-one image restoration has emerged as a practical and promising low-level vision task for real-world applications. In this context, the key issue lies in how to deal with different types of degraded images simultaneously. Existing methods fit joint regression models over multi-domain degraded-clean image pairs of different degradations. However, due to the severe ill-posedness of inverting heterogeneous degradations, they often struggle with thoroughly perceiving the degradation semantics and rely on paired data for supervised training, yielding suboptimal restoration maps with structurally compromised results and lacking practicality for real-world or unpaired data. To break the barriers, we present a Degradation-Aware Residual-Conditioned Optimal Transport (DA-RCOT) approach that models (all-in-one) image restoration as an optimal transport (OT) problem for unpaired and paired settings, introducing the transport residual as a degradation-specific cue for both the transport cost and the transport map. Specifically, we formalize image restoration with a residual-guided OT objective by exploiting the degradation-specific patterns of the Fourier residual in the transport cost. More crucially, we design the transport map for restoration as a two-pass DA-RCOT map, in which the transport residual is computed in the first pass and then encoded as multi-scale residual embeddings to condition the second-pass restoration. This conditioning process injects intrinsic degradation knowledge (e.g., degradation type and level) and structural information from the multi-scale residual embeddings into the OT map, which thereby can dynamically adjust its behaviors for all-in-one restoration. Extensive experiments across five degradations demonstrate the favorable performance of DA-RCOT as compared to state-of-the-art methods, in terms of distortion measures, perceptual quality, and image structure preservation. Notably, DA-RCOT delivers superior adaptability to real-world scenarios even with multiple degradations and shows distinctive robustness to both degradation levels and the number of degradations. Source code is publicly available at: <https://github.com/xl-tang3/DA-RCOT>.

Index Terms—All-in-One Image Restoration, Optimal Transport, Structure Preservation, Conditional Generative Models.

1 INTRODUCTION

IMAGE restoration (IR) holds a fundamental position in low-level computer vision, aiming to address the degradation (e.g., most commonly noise, blur, rain, haze, low light) in a degraded image. Traditional methods focus on designing an optimization problem that exploits priors of natural image [1], [2], [3], [4], [5] or corresponding image-induced signals such as gradients [6], [7] and residuals or noise maps [8], [9], [10]. Recent advances in deep learning techniques [11], [12], [13], [14] have triggered great achievements in image restoration, in which most methods [15], [16], [17], [18], [19], [20], [21], [22], [23] train task-specific restoration models over degraded-clean image pairs of a single known degradation. However, this specificity limits their practicability in real-world applications, e.g., autonomous navigation [24], [25], surveillance systems [26], and digital photography [27], where varied and unexpected degradations usually occur. Therefore, there is an emerging field known as “All-in-One” image restoration (AIR) that aims to address different degradations simultaneously.

To tackle the AIR problem, several works [28], [29], [30], [31], [32], [33], [34] directly fit joint regression models over multi-domain degraded-clean image pairs, minimizing pixel-wise distortion measures such as L_1 or L_2 distances. Particularly, these methods derive degradation embeddings from the degraded image as task indicators, enabling the

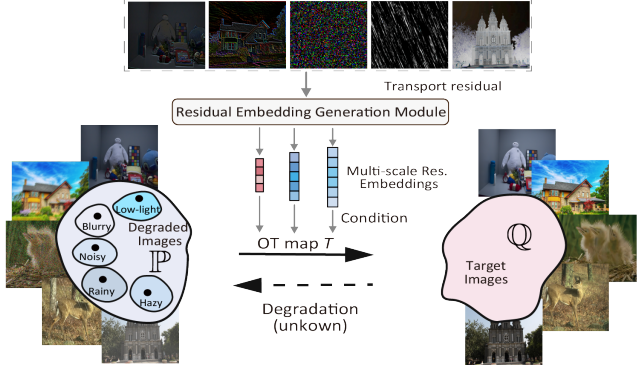
model to perform appropriate restoration while perceiving the degradation type. However, the severe ill-posedness of the regression with heterogeneous degradations still poses unique challenges for these methods, including perceiving the degradation (type and level) inadequately and leading to “average” or suboptimal restoration maps. Consequently, they tend to produce results with compromised structural details [35], [36], [37], e.g., distorted color and excessively smoothed textures (see Figure 1 (b)). Moreover, existing AIR methods rely on large amounts of paired data for supervised learning, which is usually conducted using synthetic data due to the difficulty in acquiring real-world degraded-clean pairs. As a result, the learned models tend to over-fit to the synthetic data and are vulnerable in real-world scenarios, where the availability of real-world image pairs, coupled with the complexity and diversity of real-world degradations, further hinders their applicability.

The challenges of AIR boil down to: *i*) seeking the optimal transformation of heterogeneous degraded images into clean ones while *ii*) properly perceiving the degradation semantics and prompting the preservation of visual structures, and *iii*) extending to unpaired or partially paired data.

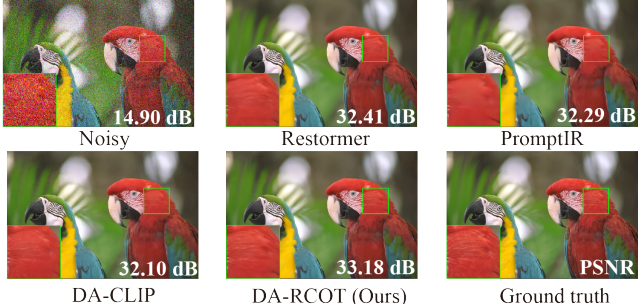
To address these challenges, this work is motivated to tackle the AIR problem from an optimal transport (OT) perspective for both unpaired and paired settings. The core idea is to seek the OT map that minimizes the transport distance between the distribution of multi-domain degraded images and the distribution of clean images, while informing the OT map with the novel transport residual (i.e., the domain gap between degraded and clean images) that contains

• The authors are with School of Mathematics and Statistics, Xi'an Jiaotong University, Shaanxi, P.R. China. E-mail: {tangxl, hexiaoyi, huxin7020,}@stu.xjtu.edu.cn, {xianggu, jiansun}@xjtu.edu.cn.

(Corresponding author: Jian Sun.)



(a) Core idea: DA-RCOT uses multi-scale transport residual embeddings as conditions for the optimal transport (OT) map to reverse multiple unknown degradations.



(b) Denoising example: DA-RCOT produces a result with better structural content.

Fig. 1. (a) The core idea of DA-RCOT is to model AIR as an OT problem and then condition the OT map with the customized multi-scale residual embeddings, yielding a degradation-aware and structure-preserving DA-RCOT map. (b) A denoising demo under noise level $\sigma = 50$. DA-RCOT produces a noise-free image with more faithful textures.

degradation-specific knowledge about the degradation and image structures (see Figure 1 (a)). In this sense, the computed OT map has the potential to perceive the degradation (type and level) and further preserve the structural contents.

Specifically, we present a Degradation-Aware Residual-Conditioned Optimal Transport (DA-RCOT) approach, introducing the novel transport residual as a degradation-specific cue for both the transport cost and the transport map. Firstly, we formalize AIR as an OT problem between the distribution of multi-domain degraded images and the distribution of clean images with a Fourier residual-guided OT (FROT) objective that exploits the frequency patterns of the residual for the transport cost. Secondly and most crucially, we design the transport map as a two-pass DA-RCOT map, in which the transport residual is computed in the first pass and then encoded as multi-scale residual embeddings to condition the second-pass restoration. This multi-scale conditioning mechanism injects intrinsic degradation knowledge (e.g., degradation type and level) and structural information from the multi-scale residual embeddings into the OT map, which thereby can dynamically adjust its behaviors for structure-preserving all-in-one restoration.

Our contributions can be mainly summarized as follows:

- We advocate an OT solution dubbed DA-RCOT for AIR, learning to transform the distribution of multi-domain degraded images to that of clean ones with a minimal cost. Uniquely, DA-RCOT introduces the transport residual as a degradation-specific cue for both the transport cost and transport map.
- We integrate the degradation knowledge into the

transport cost by exploiting the frequency patterns of transport residuals, yielding the FROT objective.

- We design the transport map as a two-pass DA-RCOT map, which dynamically conditions the OT map with degradation-specific low-level and high-level features from the multi-scale residual embeddings, enhancing its capability to perceive the degradation semantics and preserve the structures.
- Extensive experiments on synthetic and real-world data across five degradations show that DA-RCOT achieves state-of-the-art performance in all-in-one and task-specific settings. DA-RCOT also exhibits superior generalization to unseen degradation levels and robustness to the number of degradation types.

This work extends our conference paper [38] published at ICML. In the previous version, we learned a separate model based on OT theories to address single degradation, using single-scale residual embedding for structure preservation. In this work, we address the more challenging All-in-One problem by learning a unified OT map to handle different types of degradations simultaneously. Moreover, we extract multi-scale residual embeddings to condition the OT map for degradation-aware restoration. Specifically, we additionally make the following contributions: 1) We formulate AIR as an OT problem that seeks the optimal transportation from the distribution of multi-domain degraded images to that of the clean ones. 2) We employ gating-based Transformer blocks with a contrastive loss to extract multi-scale residual embeddings as conditions, which enhance the OT map with abundant degradation semantics and structural information. 3) We perform extensive experiments under AIR setting on a mixed dataset collected from multiple benchmarks, including Rain100L [39] for deraining, BSD68 [40] for denoising, SOTS [41] for dehazing, GoPro [42] for deblurring, and LOL [43] for low-light enhancement. The results substantiate the effectiveness of the proposed method and demonstrate its robustness against varying degradation numbers and unseen degradation levels as compared to the conference version and other AIR methods.

2 RELATED WORKS

2.1 Image Restoration

Task-specific Image Restoration. Task-specific IR focuses on learning separate models over degraded-clean image pairs to handle single degradation. A primary body of works [18], [19], [20], [21], [22], [23], [44], [45], [46], [47] are driven by efficient network architectures, optimizing the model under pixel-wise L_1 or L_2 distances to produce deterministic results, which often yields decent quantitative performance. Another line of task-specific methods tackles image restoration from a distribution-fitting perspective with deep generative models [48], [49], [50], [51], [52] and utilizes the degraded input as a condition for generation. RoCGAN [50] adapts CGAN [51] and uses high-quality data for supervised training of the restoration model. Ambient-GAN [52] generates clean images from noisy input, assuming the degradation satisfies certain constraints. Recently, diffusion models have emerged as a promising approach for generation. SR3 [53] conditions diffusion models on degraded images during training. Snips [54], DDRM [55],

and DPS [56] assume the degradation and its parameters are known at test time. IDM [57] introduces a scale-adaptive condition on low-resolution images to achieve high-fidelity super-resolution, while IR-SDE [22] proposes a loss function based on maximum likelihood to train a mean-reverting score-based model. These methods, which use the degraded image as a condition for posterior distribution sampling, generally produce photo-realistic results. However, they rarely seek the optimal transformation between distributions and often disregard extra degradation knowledge for guidance. Moreover, they rely on large amounts of paired data for training regression models, and thus are prone to “average” results with compromised image structures.

All-in-One Image Restoration. As compared to task-specific IR, AIR exhibits more potential for real-world applications but poses a unique challenge of addressing multiple types of degradations simultaneously. Current methods focus on how to extract informative degradation semantics from degraded input to promote task identification. AirNet [29] trains an extra encoder using contrastive learning to extract degradation embeddings from degraded images, which are then used to guide the restoration. IDR [31] breaks down image degradations into their physical principles and implements AIR using a two-stage meta-learning based approach. PromptIR [32] employs a learnable visual prompt module to adaptively encode the information of degradation type and further guide the restoration. DA-CLIP [33] uses the text embeddings from the fixed CLIP text encoder to adapt corresponding content embeddings and prompt-based degradation embeddings, which are subsequently integrated into large-scale restoration frameworks for AIR. These methods fit L_1 - or L_2 -based regression models and derive degradation embeddings from the degraded images, which often result in an inadequate perception of the degradation and lead to suboptimal restoration maps.

On the contrary, our DA-RCOT seeks the OT map to transform the multi-domain degraded images into clean ones. Meanwhile, we introduce the novel transport residual as a degradation-specific cue for both the transport cost and transport map, promoting the OT map to adaptively perceive the degradation semantics and structural information.

2.2 Optimal Transport in Generative Models

OT problem seeks to determine the optimal *transport map* (Monge Problem [58], also known as MP) or *transport plan* (Kantorovich Problem [59], also known as KP) to transform a distribution into another with the minimal cost.

Recently, OT has been presented as a powerful toolkit or framework for machine learning, especially in the field of generative models. A majority of generative models (e.g., WGAN [60], WGAN-GP [61]) use OT cost as the loss for the generative network. A different set of approaches computes OT maps or plans for generative modeling. OTCS [62] computes optimal transport plans to guide the training of the conditional score-based diffusion model for super-resolution and translation. NOT [63], KNOT [64] estimate OT maps and plans using neural networks under the duality framework and apply their method to unpaired image translation. OTUR [65] relaxes the transport constraint in Monge formulation with a Wasserstein-1 discrepancy between the target distribution and the transported distribu-

tion from noisy input. Despite pioneering the way of modeling domain translation as an OT problem, these methods rarely incorporate the degradation knowledge and empirically use a pixel-wise L_2 transport cost which may not serve as an efficient metric over complex degraded/clean image manifolds. In contrast, our DA-RCOT integrates the degradation-specific transport residual and its multi-scale embeddings into the OT framework, resulting in the FROT objective and degradation-aware DA-RCOT map for AIR.

3 PRELIMINARIES

Notation. Let Y and X be Polish spaces, and let $\mathcal{P}(Y)$ and $\mathcal{P}(X)$ denote the corresponding sets of probability measures on these spaces. We define $\Pi(\mathbb{P}, \mathbb{Q})$ as the set of all joint probability distributions on $Y \times X$ with marginals \mathbb{P} and \mathbb{Q} . For any measurable map $T : Y \rightarrow X$, the push-forward operator associated with T is denoted as $T_\#$. We use $\|\cdot\|$ to represent the standard Euclidean norm unless specified otherwise. Lastly, the space of functions on Y that are integrable with respect to \mathbb{Q} is denoted by $L^1(\mathbb{Q})$.

Given two distributions $\mathbb{P} \in \mathcal{P}(X)$ and $\mathbb{Q} \in \mathcal{P}(Y)$, along with a transport cost $c : Y \times X \rightarrow \mathbb{R}_+$, the OT problem seeks the least-effort transport from \mathbb{P} to \mathbb{Q} .

Definition 1 (Transport map): $T : Y \rightarrow X$ is a transport map that transports \mathbb{P} to \mathbb{Q} if

$$\mathbb{P}(A) = \mathbb{Q}(T^{-1}(A)),$$

for all \mathbb{P} -measurable sets A .

Definition 2 (MP): the Monge problem [58] for optimal transport can be formulated as follows:

$$\text{MP-Cost}(\mathbb{P}, \mathbb{Q}) \triangleq \inf_{T_\# \mathbb{P} = \mathbb{Q}} \int_Y c(y, T(y)) d\mathbb{P}(y), \quad (1)$$

where $T : Y \rightarrow X$ is a transport map that pushes forward \mathbb{P} to \mathbb{Q} , denoted as $T_\# \mathbb{P} = \mathbb{Q}$. The map T^* attaining the infimum is called the *optimal transport map*, which is taken over all the transport maps. Since the map T satisfying $T_\# \mathbb{P} = \mathbb{Q}$ sometimes does not exist, Kantorovich proposes the convex relaxation of the above Monge problem.

Definition 3 (KP): the Kantorovich problem [59] for optimal transport can be formulated as follows:

$$\text{KP-Cost}(\mathbb{P}, \mathbb{Q}) \triangleq \inf_{\pi \in \Pi(\mathbb{P}, \mathbb{Q})} \int_{Y \times X} c(y, x) d\pi(y, x), \quad (2)$$

where $\pi \in \Pi(\mathbb{P}, \mathbb{Q})$ is a transport plan, i.e., the joint distribution on $Y \times X$ whose marginals are \mathbb{P} and \mathbb{Q} . The plan π^* attaining the infimum is called the *optimal transport plan*, which is taken over all the transport plans.

Definition 4 (DP): KP has the dual form [66]:

$$\text{DP-Cost}(\mathbb{P}, \mathbb{Q}) = \sup_{\varphi} \int_Y \varphi^c(y) d\mathbb{P}(y) + \int_X \varphi(x) d\mathbb{Q}(x), \quad (3)$$

where $\varphi^c(y) = \inf_{x \in X} [c(x, y) - \varphi(x)]$ is the c -transform of φ and the optimal potential φ^* is taken over all $\varphi \in L^1(\mathbb{Q})$.

4 METHOD

In this section, we present DA-RCOT, an OT framework to learn a structure-preserving and degradation-aware OT map for AIR. The key idea is to model AIR as an OT problem and introduce the transport residual as a degradation-specific cue for both the transport cost and transport map.

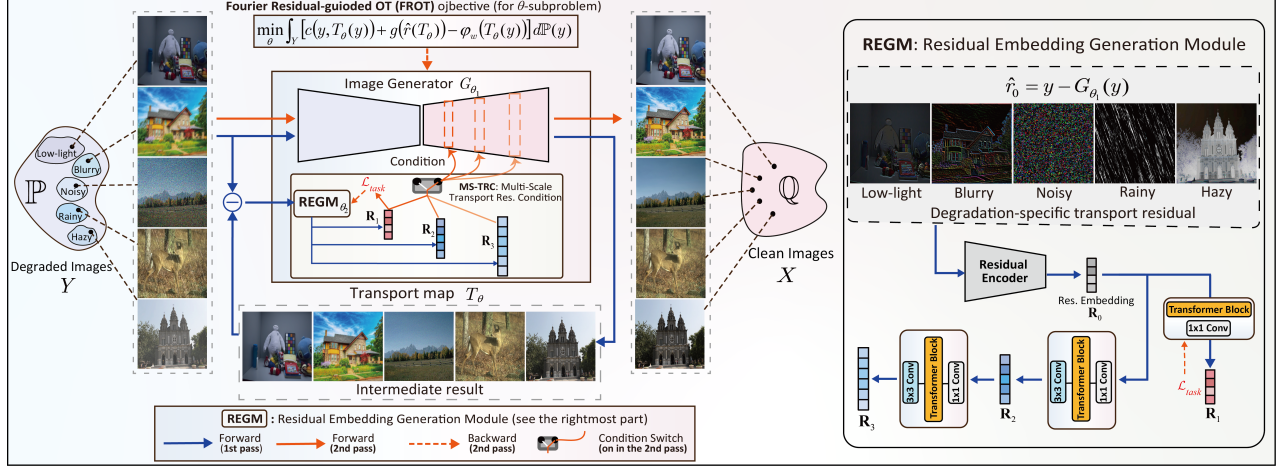


Fig. 2. Overview of the DA-RCOT framework for AIR. DA-RCOT integrates the transport residual into the transport cost, yielding the FROT objective; and more crucially, into the transport map via a two-pass conditioning process. The first pass unconditionally generates an intermediate result along with the residual \hat{r}_0 . Then the residual is encoded and adapted as multi-scale embeddings $\{R_i\}_{i=1,2,3}$ to condition the second-pass restoration.

Method overview. We first model AIR as an OT problem, exploiting the frequency patterns of the residual, yielding the FROT objective that measures the distance between the distribution of multi-domain degraded images and the clean one (section 4.1). Secondly, we integrate the degradation-specific knowledge from the multi-scale residual embeddings into the transport map via a two-pass conditioning process (section 4.2), in which the transport residual is computed in the first pass and then encoded as multi-scale residual embeddings to condition the second-pass restoration (see Figure 2). Section 4.3 illustrates the learning of multi-scale residual embeddings, while section 4.4 presents the t-SNE visualization of the dense residual embeddings for task identification. In section 4.5, we summarize the algorithm for computing the DA-RCOT map by adversarially training two neural networks to solve the minimax problem.

4.1 Residual-guided OT formulation for AIR

Let \mathbb{P} and \mathbb{Q} represent the distributions of the degraded image domain Y and clean image domain X , respectively. In the context of AIR, the degraded image domain Y contains multi-domain images of different degradations. To incorporate the degradation knowledge in the OT framework, we introduce a residual regularization term $g(\cdot)$ for the transport cost $c(y, x)$, characterizing the frequency patterns of the transport residual $r = y - x$, i.e., the degradation domain gap. Finally, we model AIR based on KP (2) with the residual regularizer in the transport cost, yielding the Fourier residual-guided OT, i.e., FROT objective:

$$\text{KP-FROT}(\mathbb{P}, \mathbb{Q}) \triangleq \inf_{\pi \in \Pi(\mathbb{P}, \mathbb{Q})} \int_{Y \times X} \tilde{c}(y, x) d\pi(y, x). \quad (4)$$

Here $\tilde{c}(y, x) = c(y, x) + g(r)$, and $c(y, x)$ is chosen to be the standard Euclidean distance, while $g(\cdot) : Y \times X \rightarrow \mathbb{R}_+$ is determined according to the frequency patterns shown in Figure 3. The transport residual r exhibits degradation-specific patterns in the image domain. While in the frequency domain, the transport residuals for degradations, except for noise, generally show sparsity. In light of this, we use ℓ_1 norm to penalize the Fourier residual for all the degradations except for noise, i.e., $g(r) = \|\mathcal{F}(r)\|_1$, and particularly use ℓ_2 norm for the denoising task.

With Eq. (4), we intend to find the OT map T^* from Y to X , which can flexibly map degraded images into clean ones. Since the duality (3) can lead us to a manageable approach, we derive the following dual form from Eq. (4)

$$\text{DP-FROT}(\mathbb{P}, \mathbb{Q}) = \sup_{\varphi} \int_Y \varphi^c(y) d\mathbb{P}(y) + \int_X \varphi(x) d\mathbb{Q}(x),$$

where $\varphi^c(y) = \inf_{x \in X} [c(x, y) + g(r) - \varphi(x)]$. Replacing the optimization of the $\varphi^c(y)$ term over target $x \in X$ with an equivalent optimization (Rockafellar interchange theorem [67], Theorem 3A) over the map of interest $T : Y \rightarrow X$, we obtain the minimax reformulation of dual form:

$$\begin{aligned} \text{DP-FROT}(\mathbb{P}, \mathbb{Q}) = \sup_{\varphi} \inf_T & \left\{ \mathcal{L}_u(T, \varphi) \triangleq \int_X \varphi(x) d\mathbb{Q}(x) \right. \\ & \left. + \int_Y [-\varphi(T(y)) + \underbrace{c(y, T(y)) + g(\hat{r}(T))}_{\text{transport cost: } \tilde{c}(y, T(y))}] d\mathbb{P}(y) \right\}, \end{aligned} \quad (5)$$

where $\hat{r}(T) = y - T(y)$ estimates the transport degradation domain gap (termed as transport residual). Notably, only unpaired data is required for solving the optimization problem (5). To further leverage the information of paired data, which is commonly encountered in practical applications, we introduce the following pair-informed FROT objective.

Pair-informed FROT Formulation. Given a paired data subset of $Y \times X$, consisting of n degraded-clean image pairs $(y_1, x^*(y_1)), \dots, (y_n, x^*(y_n))$, we can rewrite Eq. (4) with the pairwise constraint into the transport cost:

$$\inf_{\pi \in \Pi(\mathbb{P}, \mathbb{Q})} \int_{Y \times X} [\tilde{c}(y, x) + \lambda \ell(x, x^*(y))] d\pi(y, x). \quad (6)$$

Similarly to the previous steps, from Eq. (6) we can derive the minimax problem under such pairwise constraints, and the corresponding paired FROT objective function is

$$\begin{aligned} \mathcal{L}_p(T, \varphi) \triangleq & \int_X \varphi(x) d\mathbb{Q}(x) + \int_Y [-\varphi(T(y)) \\ & + \underbrace{c(y, T(y)) + g(\hat{r}(T)) + \lambda \ell(T(y), x^*(y))}_{\text{transport cost: } \tilde{c}_{x^*}(y, T(y))}] d\mathbb{P}(y). \end{aligned} \quad (7)$$

The function $\ell : Y \times X \rightarrow \mathbb{R}_+$ is a loss metric measuring the distance between samples. In our experiments, we employ

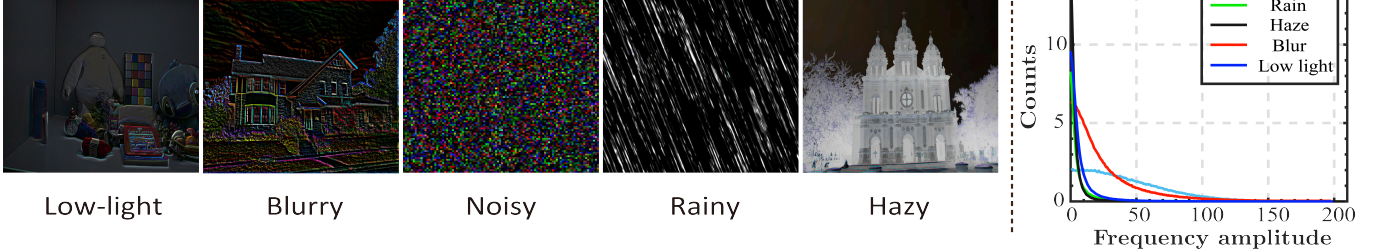


Fig. 3. Left: Visual examples of the transport residual r . Right: Counts of the frequency amplitude of residuals for five types of degradation. For all degradations except for the noise, the residuals are generally sparse in the Fourier domain. The curves are averaged with 40 degraded-clean pairs.

the ℓ_1 norm, i.e., $\ell(x, \hat{x}) = \|x - \hat{x}\|_1$. For simplicity, we denote the transport cost terms in (5) and (7) with $\tilde{c}(y, T(y))$ and $\tilde{C}_{x^*}(y, T(y))$, then the unpaired and paired FROT minimax problems can be simplified as:

$$\begin{aligned} \text{DP-FROT}(\mathbb{P}, \mathbb{Q}) = \sup_{\varphi} \inf_T \left\{ \mathcal{L}_u(T, \varphi) \triangleq \int_X \varphi(x) d\mathbb{Q}(x) \right. \\ \left. + \int_Y [\tilde{c}(y, T(y)) - \varphi(T(y))] d\mathbb{P}(y) \right\} \quad (\text{Unpaired}), \end{aligned} \quad (8)$$

$$\begin{aligned} \text{DP-FROT}(\mathbb{P}, \mathbb{Q}) = \sup_{\varphi} \inf_T \left\{ \mathcal{L}_p(T, \varphi) \triangleq \int_X \varphi(x) d\mathbb{Q}(x) \right. \\ \left. + \int_Y [\tilde{C}_{x^*}(y, T(y)) - \varphi(T(y))] d\mathbb{P}(y) \right\} \quad (\text{Paired}), \end{aligned} \quad (9)$$

We can show that solving the FROT minimax problems provides OT maps, for both unpaired and paired cases.

Proposition 1. (Saddle points of FROT provide OT maps). For any optimal potential $\varphi_1^* \in \arg \sup_{\varphi} \mathcal{L}_u(T, \varphi_1)$ and $\varphi_2^* \in \arg \sup_{\varphi} \mathcal{L}_p(T, \varphi_2)$, it holds for the OT map T^* that

$$T^* \in \arg \inf_{T: Y \rightarrow X} \mathcal{L}_u(T, \varphi_1^*), \quad (10)$$

$$T^* \in \arg \inf_{T: Y \rightarrow X} \mathcal{L}_p(T, \varphi_2^*). \quad (11)$$

Proof. We provide proof for the unpaired case (10), and the proof for the paired case (11) is identical, so it is omitted. According to the Monge problem (1), the MP-FROT objective under transport cost \tilde{c} is

$$\text{MP-FROT}(\mathbb{P}, \mathbb{Q}) = \inf_{T: \# \mathbb{P} = \mathbb{Q}} \int_Y \tilde{c}(y, T(y)) d\mathbb{P}(y). \quad (12)$$

Since φ_1^* is the optimal potential, we have $\inf_T \mathcal{L}(T, \varphi_1^*) = \text{FROT}(\mathbb{P}, \mathbb{Q})$. For the OT map T^* in (12), using $T^* \# \mathbb{P} = \mathbb{Q}$ and the change of variables $T^*(y) = x$, we deduce

$$\int_Y \varphi_1^*(T^*(y)) d\mathbb{P}(y) = \int_X \varphi_1^*(x) d\mathbb{Q}(x).$$

Substituting this equation into $\mathcal{L}_u(T, \varphi_1)$, we obtain

$$\begin{aligned} \mathcal{L}_u(T^*, \varphi_1^*) &= \int_Y \tilde{c}(y, T^*(y)) d\mathbb{P}(y) \\ &= \inf_{T: \# \mathbb{P} = \mathbb{Q}} \int_Y \tilde{c}(y, T(y)) d\mathbb{P}(y) = \text{MP-FROT}(\mathbb{P}, \mathbb{Q}). \end{aligned} \quad (13)$$

According to Pratelli [68] and Villani [66], since \tilde{c} is continuous and (X, \mathbb{P}) is Polish without atoms, we have

$$\text{MP-FROT}(\mathbb{P}, \mathbb{Q}) = \text{KP-FROT}(\mathbb{P}, \mathbb{Q}) = \text{DP-FROT}(\mathbb{P}, \mathbb{Q}).$$

This result, together with Eq. (13), demonstrates that $T^* \in$

$\arg \inf_T \mathcal{L}_u(T, \varphi_1^*)$. For the paired case with \mathcal{L}_p and φ_2^* , we immediately reach the conclusion by replacing \tilde{c} with \tilde{C}_{x^*} , which is also continuous, thus completing the proof. \square

Proposition 1 affirms the feasibility of solving the minimax problems to acquire an optimal pair, constituting an OT map from \mathbb{P} to \mathbb{Q} . For general \mathbb{P} and \mathbb{Q} , given some optimal potential φ^* , the set $\arg \inf_T$ may encompass not only the OT map T^* but also other saddle points, which are capable of delivering decent performance as in experiments (section 5). To tackle the minimax problems, we parameterize the transport map T and potential φ using two neural networks T_θ and φ_ω , and then perform adversarial training to optimize their parameters against each other.

4.2 Learning Degradation-Aware OT Map Conditioned on Multi-Scale Residual Embeddings

In order to enable the OT map to perceive the degradation semantics for AIR while preserving more image structures, we design the transport map as the two-pass DA-RCOT map by taking the multi-scale residual embeddings as its additional conditions. The transport residuals convey degradation-specific patterns related to both the degradation (type and level) and image structures (see Figure 3), which could be leveraged to inform the OT map for degradation-aware and structure-preserving restoration. To this end, the parameterized transport map T_θ is implemented to comprise two components: an image generator G with parameters θ_1 , and a multi-scale residual embeddings generation module (REGM) with parameters θ_2 . We next elaborate the two-pass restoration process of the DA-RCOT map (see the overall framework shown in Figure 2).

Two-pass DA-RCOT map for restoration. Given a degraded image y from the heterogeneous degraded image domain Y , the first pass of the DA-RCOT map unconditionally generates an intermediate restored result $\hat{x}_0 = G(y; \theta_1)$ via the generator and calculates the corresponding intermediate transport residual $\hat{r}_0 = y - \hat{x}_0$. Then the residual \hat{r}_0 is fed into REGM to produce multi-scale residual embeddings $\{\mathbf{R}_i\}_{i=1,2,3}$. In the second pass, these embeddings serve as conditions for the generator G , yielding the refined result $T_\theta(y) = G(y | \mathbf{R}_1, \mathbf{R}_2, \mathbf{R}_3; \theta_1)$. This process boils down to:

$$\begin{aligned} \hat{r}_0 &= y - G(y; \theta_1); [\mathbf{R}_1, \mathbf{R}_2, \mathbf{R}_3] = \text{REGM}(\hat{r}_0; \theta_2); \\ T_\theta(y) &= G(y | \mathbf{R}_1, \mathbf{R}_2, \mathbf{R}_3; \theta_1). \end{aligned} \quad (14)$$

where $\{\mathbf{R}_i\}_{i=1,2,3}$ serve as conditions for different scales of the generator G , with \mathbf{R}_1 specifically used at the dense scale to enhance the semantics of heterogeneous degradations.

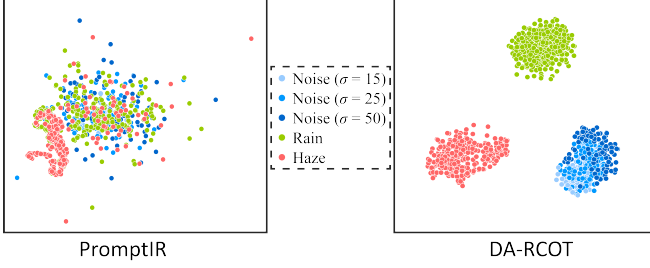


Fig. 4. The t-SNE visual comparison of the degradation embeddings from PromptIR [32] and DA-RCOT. As compared to the prompt-based embeddings of PromptIR [32], the residual embeddings \mathbf{R}_1 of DA-RCOT are clearly separated according to the specific tasks. Particularly, the residual embeddings w.r.t. different levels of noise are clustered together but also exhibit level-specific positional relationships.

Learning multi-scale residual embeddings with REGM

To extract the multi-scale residual embeddings $\{\mathbf{R}_i\}_{i=1,2,3}$, the REGM incorporates some gating-based Transformer blocks that selectively permit the propagation of essential features across different scales. The blocks consist of two key sub-modules: Multi-Dconv head transposed attention (MDTA), and Gated-Dconv feedforward network (GDFN) [19]. MDTA uses depth-wise convolutions to emphasize the local image structures, while GDFN selectively transforms features with a gating mechanism that suppresses the less informative features and allows only useful ones to propagate. The propagation process of REGM (see the rightmost of Figure 2) is summarized as

$$\begin{aligned} \mathbf{R}_0 &= \text{Encoder}(\hat{r}_0); \quad \mathbf{R}_1 = (\text{GDFN}(\text{MDTA}(\text{Conv}_{1 \times 1}(\mathbf{R}_0)))); \\ \mathbf{R}_2 &= \text{Conv}_{3 \times 3}(\text{GDFN}(\text{MDTA}(\text{Conv}_{1 \times 1}(\mathbf{R}_0)))); \\ \mathbf{R}_3 &= \text{Conv}_{3 \times 3}(\text{GDFN}(\text{MDTA}(\text{Conv}_{1 \times 1}(\mathbf{R}_2)))) \quad (15) \end{aligned}$$

Moreover, the work [69] observes that the shallow layers of U-shaped architecture capture low-level structural features such as color and textures, while the deep layers provide semantic guidance. In light of this, we employ a contrastive loss that promotes \mathbf{R}_1 to emphasize the task semantic features of the degradation. Specifically, for the residual embedding \mathbf{R}_1^k from k -th task among K tasks, the positive samples are embeddings from other degraded inputs of k -th task, denoted as \mathbf{R}_1^{k+} ; and the negative samples are embeddings from other tasks \mathbf{R}_1^{k-} . The contrastive loss for task identification is defined as

$$\mathcal{L}_{task} = - \sum_{k=1}^K \log \frac{\sum_{\mathbf{R}_1^{k+}} \exp(\mathbf{R}_1^k \cdot \mathbf{R}_1^{k+} / \tau)}{\sum_{\mathbf{R}_1^{k+}} \exp(\frac{\mathbf{R}_1^k \cdot \mathbf{R}_1^{k+}}{\tau}) + \sum_{\mathbf{R}_1^{k-}} \exp(\frac{\mathbf{R}_1^k \cdot \mathbf{R}_1^{k-}}{\tau})} \quad (16)$$

where τ is the temperature hyper-parameter. As shown in Figure 2, the learned residual embedding \mathbf{R}_1 is utilized as the condition at the dense scale to enhance the OT map's capability to perceive the degradation semantics. Meanwhile, \mathbf{R}_2 and \mathbf{R}_3 are used at shallow layers to augment the OT map with extra low-level structural information.

4.3 Visualization on the Degradation Embeddings

To better understand the semantic nature of the residual embedding \mathbf{R}_1 , we employ t-SNE for visualizing, using 300 noisy images (100 each for $\sigma = 15, \sigma = 25, \sigma = 50$),

Algorithm 1 Computing the DA-RCOT map for AIR.

Input: degraded images $Y \sim \mathbb{P}$; clean images $X \sim \mathbb{Q}$; transport network: T_θ ; potential network: φ_w ; the number of iterations of θ per iteration of ω : n_T ;

```

1: while  $\theta$  has not converged do
2:   Sample batches  $\mathcal{Y}$  from  $Y, \mathcal{X}$  from  $X$ ;
3:    $\mathcal{L}_\varphi \leftarrow \frac{1}{|\mathcal{Y}|} \sum_{y \in \mathcal{Y}} \varphi_w(T_\theta(y)) - \frac{1}{|\mathcal{X}|} \sum_{x \in \mathcal{X}} \varphi_w(x)$ ;
4:   Update  $w$  by using  $\frac{\partial \mathcal{L}_\varphi}{\partial w}$ ;
5:   for  $t = 0, \dots, n_T$  do
6:     Compute  $\{\mathbf{R}_i\}_{i=1,2,3}$  via (15);
7:     Compute  $\mathcal{L}_{task}$  via (16);
8:     Compute  $T_\theta(y)$  via (14);
9:     if there exist paired samples then
10:       $\mathcal{L}_T \leftarrow \frac{1}{|\mathcal{Y}|} \sum_{y \in \mathcal{Y}} [\tilde{C}_{x^*}(y, T_\theta(y)) - \varphi_\omega(T_\theta(y))]$ ;
11:    else
12:       $\mathcal{L}_T \leftarrow \frac{1}{|\mathcal{Y}|} \sum_{y \in \mathcal{Y}} [\tilde{c}(y, T_\theta(y)) - \varphi_\omega(T_\theta(y))]$ ;
13:    end if
14:     $\mathcal{L} \leftarrow \mathcal{L}_T + \gamma \mathcal{L}_{task}$ ;
15:    Update  $\theta$  by using  $\frac{\partial \mathcal{L}}{\partial \theta}$ ;
16:   end for
17: end while

```

300 rainy images, and 300 haze images. Embeddings from different sources are marked with distinct colors.

We compare our residual embeddings with the prompt-based degradation embeddings from the state-of-the-art method PromptIR [32]. As shown in Figure 4, compared to the prompt-based degradation embeddings in PromptIR [32], the residual embeddings \mathbf{R}_1 of DA-RCOT are clearly separated according to specific tasks. Particularly, the residual embeddings w.r.t. different levels of noise are clustered together but also exhibit level-specific positional relationships. This observation demonstrates that \mathbf{R}_1 not only captures relatively precise semantics of the degradation but also retains sensitivity to perceive varying degradation levels, which enhances its robustness to handle diverse degradations in the presence of level shifts.

4.4 Overall Training Algorithm

After parameterizing T_θ and φ_w , the objective functions of minimax problems (10) and (11) can be rewritten as

$$\begin{aligned} \mathcal{L}_u(\omega, \theta) &= \mathbb{E}_{x \sim \mathbb{Q}} [\varphi_w(x)] + \mathbb{E}_{y \sim \mathbb{P}} [\tilde{c}(y, T_\theta(y)) - \varphi_\omega(T_\theta(y))], \\ \mathcal{L}_p(\omega, \theta) &= \mathbb{E}_{x \sim \mathbb{Q}} [\varphi_w(x)] + \mathbb{E}_{y \sim \mathbb{P}} [\tilde{C}_{x^*}(y, T_\theta(y)) - \varphi_\omega(T_\theta(y))]. \quad (17) \end{aligned}$$

For these two problems, we train the networks T_θ and φ_w by respectively minimizing and maximizing the objectives \mathcal{L}_u or \mathcal{L}_p , i.e., $\max_\omega \min_\theta \mathcal{L}_u(\omega, \theta)$ or $\max_\omega \min_\theta \mathcal{L}_p(\omega, \theta)$. This can be implemented by adversarially training T_θ and φ_w , in which we estimate the expectation using mini-batch data in each training step. The training algorithm for computing the DA-RCOT map is summarized in Algorithm 1.

5 EXPERIMENTS

We evaluate the proposed DA-RCOT on both real-world and synthetic datasets under two distinct configurations: 1) All-in-One and 2) Task-specific. In the All-in-One configuration, a single model is trained to handle multiple types of

TABLE 1

The *All-in-One* comparison of our DA-RCOT with the state-of-the-art methods on **three** degradations. The metrics are reported in the form of PSNR(\uparrow)/SSIM(\uparrow)/LPIPS(\downarrow)/FID(\downarrow). (*) indicates the method is performed in an unpaired setting.

Method	Dehazing		Deraining		Denoising		Average
	SOTS	Rain100L	BSD68 $_{\sigma=15}$	BSD68 $_{\sigma=25}$	BSD68 $_{\sigma=50}$		
Unpaired	CycleGAN* [70]	24.26/0.923/0.066/48.33	30.12/0.912/0.087/65.24	30.25/0.872/0.101/89.23	26.75/0.776/0.174/112.6	23.45/0.702/0.234/152.5	26.97/0.837/0.132/93.57
	WGAN-GP* [61]	25.28/0.929/0.043/34.98	32.87/0.970/0.066/51.12	30.87/0.869/0.104/71.32	28.12/0.801/0.158/97.22	26.18/0.722/0.216/130.2	28.66/0.857/0.117/76.97
	OTUR* [65]	25.56/0.935/0.046/39.59	32.83/0.934/0.076/58.91	31.17/0.889/0.099/76.13	28.66/0.820/0.153/92.54	26.53/0.744/0.211/126.7	28.95/0.864/0.117/78.76
	RCOT* [38]	<u>27.02/0.945/0.038/32.26</u>	<u>33.56/0.945/0.055/37.25</u>	<u>31.95/0.902/0.085/61.29</u>	<u>29.33/0.834/0.135/82.15</u>	<u>26.98/0.757/0.201/113.2</u>	<u>29.77/0.877/0.103/65.23</u>
Paired	DA-RCOT*	<u>27.64/0.964/0.027/23.17</u>	<u>33.82/0.960/0.032/28.54</u>	<u>32.28/0.918/0.064/40.58</u>	<u>30.12/0.864/0.122/72.21</u>	<u>27.16/0.779/0.189/101.7</u>	<u>30.20/0.897/0.087/53.24</u>
	MPRNet [18]	25.43/0.956/0.038/28.15	33.66/0.955/0.057/33.65	33.50/0.925/0.084/52.87	30.89/0.880/0.127/79.53	27.48/0.778/0.201/121.9	30.19/0.899/0.101/63.23
	Restormer [19]	29.92/0.970/0.035/22.29	35.64/0.971/0.036/33.97	33.81/0.932/0.078/42.61	31.00/0.880/0.113/74.62	27.85/0.792/0.198/117.6	31.62/0.909/0.092/58.22
	IR-SDE [22]	29.35/0.961/0.029/19.80	34.87/0.958/0.031/30.36	32.89/0.903/0.068/35.51	30.56/0.861/0.107/68.15	27.22/0.769/0.195/107.6	30.98/0.890/0.086/52.29
	DL [28]	26.92/0.931/0.042/30.05	32.62/0.931/0.058/39.29	33.05/0.914/0.079/56.13	30.41/0.861/0.129/81.51	26.90/0.740/0.204/123.2	29.98/0.875/0.102/66.04
	AirNet [29]	27.94/0.962/0.030/26.71	34.80/0.962/0.054/33.28	33.92/0.933/0.066/45.67	31.26/0.888/0.110/72.74	28.00/0.797/0.194/106.6	31.18/0.908/0.091/57.00
	IDR [31]	28.68/0.968/0.018/18.55	35.99/0.968/0.025/23.65	33.89/0.932/0.063/39.13	<u>31.65/0.889/0.103/63.79</u>	28.02/0.798/0.187/102.6	31.64/0.911/0.079/49.54
	PromptIR [32]	<u>30.58/0.974/0.012/13.23</u>	36.37/0.972/0.019/16.78	<u>33.97/0.933/0.046/27.54</u>	31.29/0.888/0.090/53.69	<u>28.06/0.798/0.179/95.84</u>	32.05/0.913/0.069/41.42
	DA-CLIP [33]	30.12/0.972/0.009/8.952	35.92/0.972/0.015/13.73	33.86/0.925/0.045/25.27	31.06/0.865/0.082/48.64	27.55/0.778/0.168/89.28	31.70/0.901/0.063/37.17
	RCOT [38]	30.32/0.973/0.009/10.52	<u>37.25/0.974/0.015/12.25</u>	33.86/0.932/0.048/30.12	31.20/0.886/0.096/57.25	28.03/0.797/0.162/87.69	<u>32.13/0.912/0.067/39.57</u>
	DA-RCOT	31.26/0.977/0.007/4.058	38.36/0.983/0.008/6.154	33.98/0.934/0.038/21.05	<u>31.33/0.890/0.073/39.01</u>	28.10/0.801/0.150/80.01	32.60/0.917/0.055/30.06

TABLE 2

The *All-in-One* comparison of our DA-RCOT with the state-of-the-art methods on **five** degradations. The metrics are reported in the form of PSNR(\uparrow)/SSIM(\uparrow)/LPIPS(\downarrow)/FID(\downarrow). (*) indicates the method is performed in an unpaired setting.

Method	Dehazing		Deraining		Denoising		Deblurring	Low-light	Average
	SOTS	Rain100L	BSD68 $_{\sigma=25}$	GoPro	LOL-v1				
Unpaired	CycleGAN* [70]	20.53/0.824/0.083/69.67	22.67/0.796/0.110/82.57	26.58/0.788/0.165/107.5	18.25/0.650/0.256/102.2	16.85/0.636/0.152/176.2	20.97/0.738/0.153/107.6	25.22/0.818/0.118/83.70	25.57/0.828/0.108/69.27
	WGAN-GP* [61]	20.92/0.856/0.076/58.52	30.45/0.912/0.087/54.28	27.67/0.792/0.168/108.9	19.19/0.665/0.221/94.23	17.27/0.640/0.140/168.1	23.10/0.773/0.138/96.82		
	OTUR* [65]	21.41/0.871/0.072/57.82	30.86/0.919/0.086/53.84	28.01/0.804/0.165/108.4	19.78/0.671/0.220/93.00	17.49/0.649/0.136/167.1	23.51/0.783/0.136/96.03		
	RCOT* [38]	<u>24.55/0.914/0.052/39.62</u>	<u>32.83/0.948/0.062/54.57</u>	<u>28.65/0.813/0.147/90.29</u>	<u>21.36/0.712/0.206/79.91</u>	<u>18.73/0.705/0.127/154.1</u>	<u>25.22/0.818/0.118/83.70</u>		
Paired	DA-RCOT*	<u>24.87/0.923/0.041/30.28</u>	<u>33.19/0.953/0.054/45.72</u>	<u>28.73/0.815/0.140/83.20</u>	<u>21.85/0.727/0.188/63.26</u>	<u>19.21/0.722/0.118/123.9</u>	<u>25.57/0.828/0.108/69.27</u>	26.51/0.853/0.106/68.86	27.46/0.881/0.098/65.54
	MPRNet [18]	24.28/0.931/0.061/43.55	33.12/0.927/0.064/57.84	30.18/0.846/0.112/83.47	25.98/0.786/0.179/55.95	18.98/0.776/0.115/103.5	26.51/0.853/0.106/68.86		
	Restormer [19]	24.09/0.927/0.065/41.76	34.81/0.971/0.045/49.18	30.78/0.876/0.095/72.95	27.22/0.829/0.174/56.10	20.41/0.806/0.109/107.7	27.46/0.881/0.098/65.54		
	IR-SDE [22]	24.56/0.940/0.047/29.89	34.12/0.951/0.040/43.95	30.89/0.865/0.089/62.16	26.34/0.800/0.162/48.77	20.07/0.780/0.102/86.13	27.20/0.867/0.088/54.18		
	DL [28]	20.54/0.826/0.096/76.25	21.96/0.762/0.122/87.15	23.09/0.745/0.155/154.2	19.86/0.672/0.218/85.48	19.83/0.712/0.120/125.8	21.06/0.743/0.142/105.7		
	AirNet [29]	21.04/0.884/0.077/62.52	32.98/0.951/0.058/50.12	30.91/0.882/0.102/78.12	24.35/0.781/0.189/66.13	18.18/0.735/0.122/116.9	25.49/0.847/0.110/74.76		
	IDR [31]	25.24/0.943/0.052/33.25	35.63/0.965/0.043/45.62	<u>31.60/0.887/0.092/66.24</u>	27.87/0.846/0.178/40.83	21.34/0.826/0.108/100.6	28.33/0.893/0.095/57.31		
	PromptIR [32]	<u>30.41/0.972/0.017/20.12</u>	36.17/0.970/0.024/22.53	31.20/0.885/0.097/66.91	27.93/0.851/0.155/29.52	<u>22.89/0.829/0.098/70.32</u>	29.72/0.901/0.078/41.88		
	DA-CLIP [33]	29.78/0.968/0.014/15.26	35.65/0.962/0.022/22.24	30.93/0.885/0.089/54.12	27.31/0.838/0.143/23.34	21.66/0.828/0.095/55.81	29.07/0.896/0.073/34.15		
	RCOT [38]	30.26/0.971/0.016/16.74	<u>36.88/0.975/0.024/19.67</u>	31.05/0.882/0.099/62.12	<u>28.12/0.862/0.155/21.56</u>	22.76/0.830/0.097/61.24	<u>29.81/0.904/0.078/36.26</u>		
	DA-RCOT	<u>30.96/0.975/0.008/10.62</u>	<u>37.87/0.980/0.012/12.20</u>	<u>31.23/0.888/0.082/37.65</u>	<u>28.68/0.872/0.135/12.39</u>	<u>23.25/0.836/0.084/47.23</u>	<u>30.40/0.911/0.064/24.02</u>		

degradation, including three and five distinct degradation types on benchmark datasets. Conversely, the task-specific configuration requires the training of separate models, each dedicated to specific restoration tasks. We use PSNR/SSIM for measuring pixel-wise similarity, LPIPS [71]/FID [72] for measuring perceptual deviation, and two well-known non-reference indexes NIQE [73] and PIQE [74] to assess real-world multiple-degradation images. The best and second-best are **highlighted** and **underlined** respectively. The FID scores are calculated with 256×256 center-cropped patches.

Implementation details. We train our models under all configurations using the RMSProp optimizer with a learning rate of 1×10^{-4} for the transport network T_θ and 0.5×10^{-4} for the potential network φ_w . The temperature hyperparameter τ is empirically set as 0.07. The inner iteration number n_T is set to be 1. In all experiments, the transport map T_θ is implemented with the backbone in Restormer [19] and the potential network is the same as [75]. In the FROT objective, $c(y, x)$ is suggested as $\|y - x\|$. During training, we crop patches of size 128x128 as input. All the experiments are conducted on Pytorch with an NVIDIA 4090 GPU. For the

unpaired setting, although datasets that contain paired data are used for training, we randomly shuffle the target x and degraded input y to ensure the loss is isolated from paired information, which is a common strategy [63], [64], [65] for unpaired restoration.

Datasets. We evaluate the proposed method on benchmark datasets covering both synthetic and real-world data. For denoising, we merge BSD400 [76] and WED [77] datasets, adding Gaussian noise with levels $\sigma \in \{15, 25, 50\}$. Testing is conducted on the Kodak24 [78] and BSD68 [40] datasets. For deraining, we use the Rain100L [39] and real-world SPANet [79]. For dehazing, we employ SOTS [41] and real-world O-HAZE [80]. The deblurring and low-light enhancement tasks leverage GoPro [42] and LOL-v1 [43] datasets, respectively. For the All-in-One configuration, we merge these datasets into a mixed one with three or five degradation types for training a unified model.

5.1 All-in-One Restoration Results

We compare our All-in-One DA-RCOT map with several state-of-the-art methods including three general restoration restorers, i.e., MPRNet [18], Restormer [19], IR-SDE [22]; and

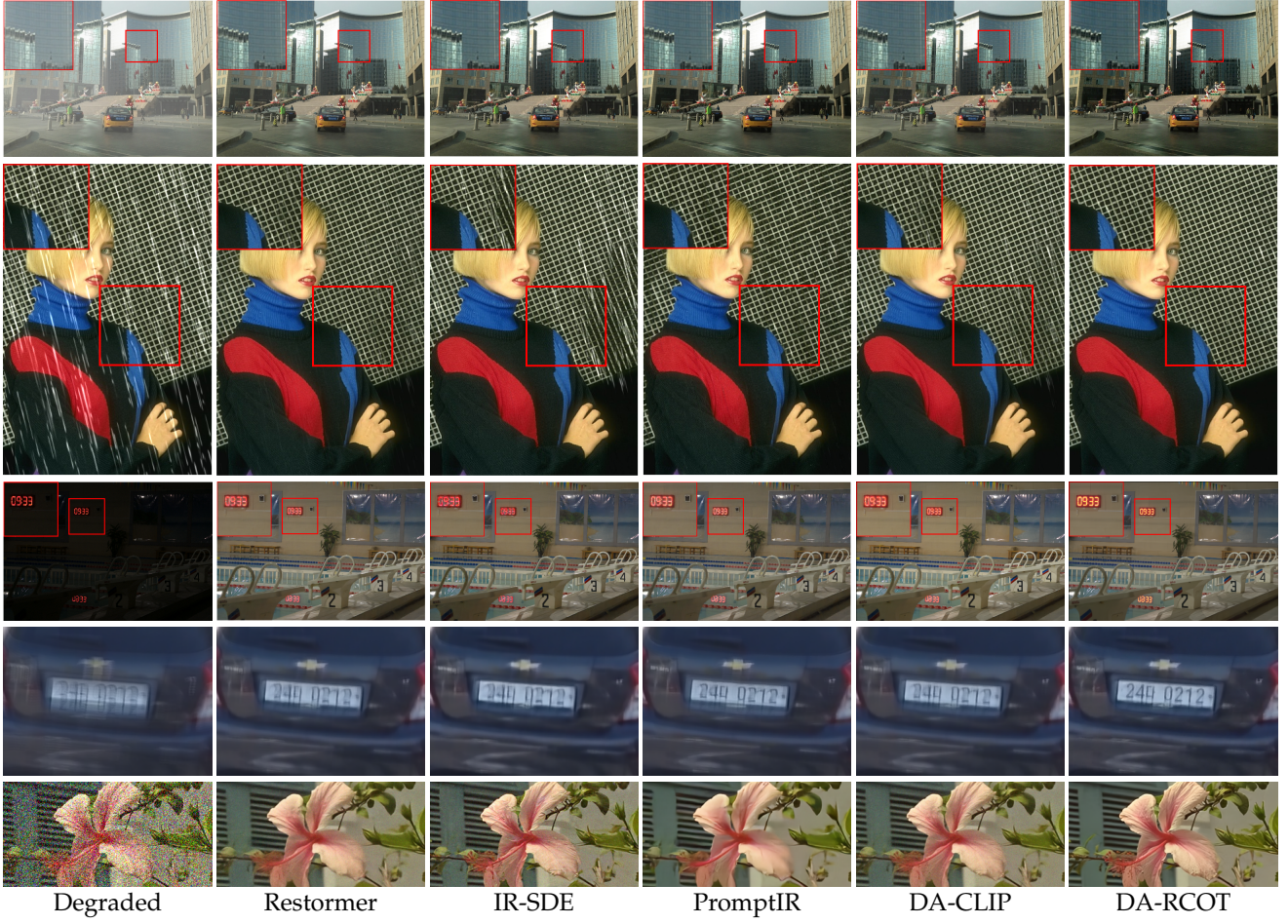


Fig. 5. Visual comparison of five-degradation All-in-One results. DA-RCOT restores sharp images with more faithful structural contents.

five specialized All-in-One models, i.e., DL [28], AirNet [29], IDR [31], PromptIR [32], DA-CLIP [33]. In particular, we also compete against the OT-based method and OTUR [65] and the GAN-based method CycleGAN [70] and WGAN-GP [61] for restoration under an unpaired setting.

Three degradations. The first comparison is performed on three degradations, i.e., dehazing, deraining, and denoising on images of noise levels $\sigma \in \{15, 25, 50\}$. Table 1 reports the quantitative results, showing that our DA-RCOT performs best under all metrics among the competitors. In the unpaired setting, our DA-RCOT outperforms the second-best method by an average of 2.11 dB in PSNR and 0.030 in LPIPS. In the paired setting, DA-RCOT outperforms other Approaches in terms of both distortion measures (PSNR and SSIM) and perceptual quality measures (LPIPS and FID), offering an average improvement of 0.55 db in PSNR compared to the PromptIR [32].

Five degradations. To evaluate the adaptability of DA-RCOT to more tasks in All-in-One setting, we extend the comparison to a five-degradation scenario, adding the tasks of deblurring and low-light enhancement. As shown in Table 2, DA-RCOT stands out with an average improvement of 0.68 dB over PromptIR [32] in PSNR and 10.13 reduction over DA-CLIP [33] in FID, which demonstrates the adaptability of the DA-RCOT map for more diverse degradations.

Figure 5 displays the visual results of the evaluated methods under five degradation scenarios. PromptIR produces results with over-smoothed structures or ar-

tifacts. DA-CLIP [33] can produce seemingly realistic results but with remaining distortion like blur and noise. In comparison, our DA-RCOT can effectively remove the degradation while preserving the image structures.

5.2 Task-specific Restoration Results

We also validate the effectiveness of DA-RCOT under task-specific configuration by training individual models over the single-degradation datasets. We evaluate the approaches for comparison on Rain100L [39] and real-world SPANet [79] for deraining, SOTS [41] and real-world O-HAZE [80] for dehazing, BSD68 [40] for denoising. For each task, we add a task-specific state-of-the-art method for each comparison, i.e., SFNet [81] for deraining, Dehazeformer [82] for dehazing, and RCD [83] for denoising.

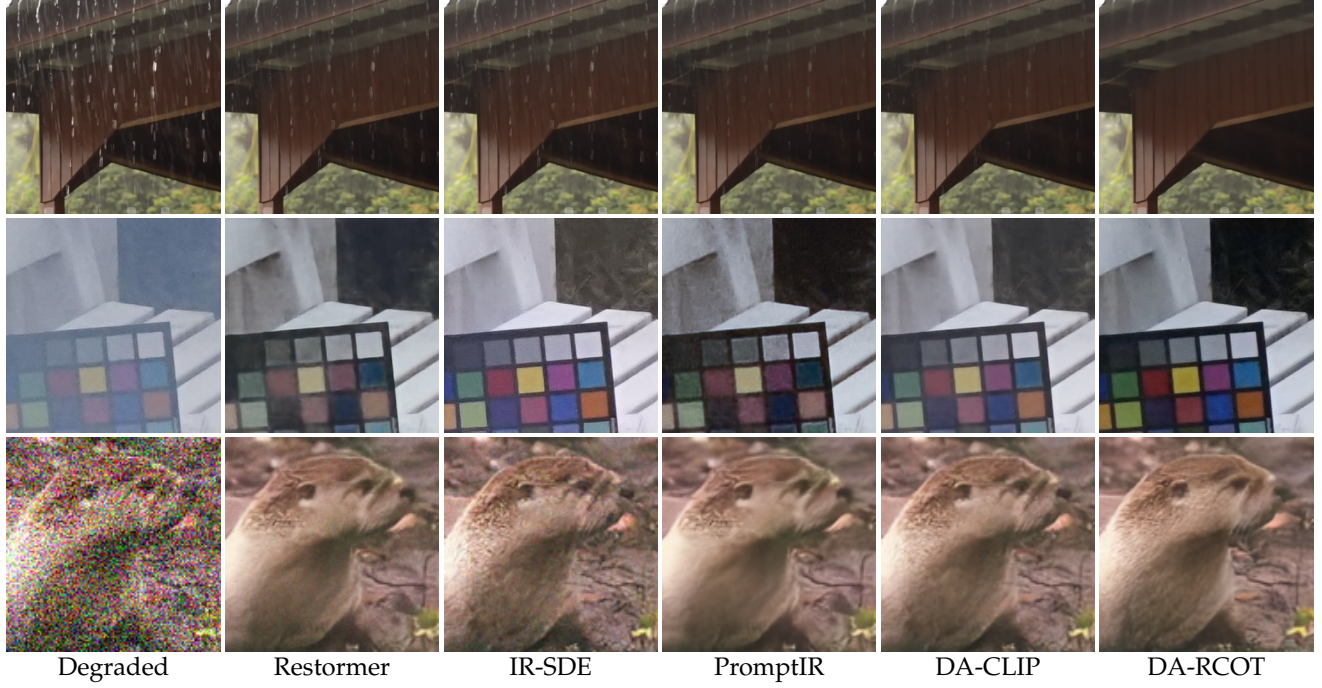
Table 3 reports the quantitative results of the restoration methods under task-specific configuration. Across all tasks, DA-RCOT consistently outperforms other approaches in all metrics. Specifically, in terms of PSNR, DA-RCOT surpasses PromptIR [32] by 1.94 dB on Rain100L and outperforms DA-CLIP [33] by 2.49 dB on SPANet. When compared to the highly competitive task-specific Dehazeformer [82] for dehazing, DA-RCOT achieves an improvement of 0.44 dB on SOTS and 2.22 dB on O-HAZE. The visual resultsParticularly, as compared to the preliminary work RCOT [38], DA-RCOT still offers a non-trivial improvement. Figure 6 displays three task-specific examples, where DA-RCOT produces cleaner results with more faithful structures (textures

TABLE 3

The Task-specific comparison on single degradations. The metrics are reported in the form of PSNR(\uparrow)/SSIM(\uparrow)/LPIPS(\downarrow)/FID(\downarrow).

(a) Deraining			(b) Dehazing		
Method	Synthetic Rain100L	Real-world SPANet	Method	Synthetic SOTS	Real-world O-HAZE
MPRNet [18]	34.95/0.964/0.039/21.61	39.52/0.967/0.021/28.13	MPRNet [18]	28.31/0.954/0.029/17.79	21.55/0.778/0.256/223.8
Restormer [19]	36.74/0.978/0.026/13.29	41.39/0.981/0.013/19.67	Restormer [19]	30.87/0.969/0.026/13.29	25.20/0.804/0.221/198.0
SFNet [81]	36.56/0.974/0.023/13.12	41.02/0.980/0.015/21.52	IR-SDE [22]	30.55/0.968/0.018/12.76	22.13/0.776/0.160/179.2
IR-SDE [22]	36.94/0.978/0.014/9.521	42.43/0.986/0.013/17.25	Dehazeformer [82]	31.45/0.978/0.021/15.54	25.56/0.812/0.209/199.3
AirNet [29]	34.90/0.977/0.035/20.96	39.67/0.969/0.019/25.62	AirNet [29]	28.52/0.956/0.027/17.22	21.42/0.774/0.231/219.3
PromptIR [32]	37.23/0.980/0.017/10.21	41.17/0.979/0.019/21.52	PromptIR [32]	31.31/0.973/0.021/16.28	25.27/0.813/0.216/217.6
DA-CLIP [33]	37.02/0.978/0.012/8.963	42.84/0.988/0.009/14.61	DA-CLIP [33]	30.88/0.974/0.009/8.657	23.86/0.782/0.158/163.8
RCOT [38]	37.73/0.981/0.013/7.551	43.98/0.994/0.011/8.457	RCOT [38]	31.52/0.976/0.014/10.05	27.10/0.838/0.155/167.7
DA-RCOT	38.73/0.985/0.007/5.013	45.33/0.997/0.006/6.289	DA-RCOT	31.89/0.978/0.007/4.058	27.78/0.845/0.140/148.5

(c) Denoising						
Method	Kodak24			BSD68		
	$\sigma = 15$	$\sigma = 25$	$\sigma = 50$	$\sigma = 15$	$\sigma = 25$	$\sigma = 50$
MPRNet [18]	34.26/0.901/0.072/41.35	31.96/0.868/0.112/43.98	28.36/0.785/0.185/73.26	33.74/0.931/0.076/39.34	30.89/0.880/0.103/59.23	27.73/0.782/0.195/103.6
Restormer [19]	34.73/0.918/0.060/24.76	32.13/0.880/0.097/33.22	29.25/0.799/0.156/64.26	34.13/0.936/0.049/25.19	31.60/0.895/0.085/49.28	28.35/0.801/0.177/88.26
IR-SDE [22]	33.92/0.898/0.068/30.11	31.40/0.842/0.089/45.56	28.03/0.721/0.145/73.66	33.14/0.907/0.050/28.22	30.46/0.856/0.086/46.30	26.98/0.737/0.172/86.40
RCD [83]	34.56/0.916/0.070/39.21	32.18/0.880/0.089/39.85	29.13/0.795/0.157/63.26	33.98/0.934/0.065/36.77	31.28/0.886/0.089/50.96	28.01/0.796/0.186/91.78
AirNet [29]	34.51/0.915/0.076/35.24	31.93/0.867/0.099/32.78	28.70/0.793/0.176/77.12	34.02/0.934/0.068/38.14	31.48/0.893/0.094/55.12	28.11/0.806/0.184/93.94
PromptIR [32]	34.85/0.926/0.054/17.52	32.25/0.883/0.091/30.91	29.49/0.809/0.154/60.42	34.26/0.937/0.046/24.77	31.71/0.897/0.085/45.45	28.49/0.813/0.172/85.46
DA-CLIP [33]	34.43/0.905/0.065/16.28	31.78/0.865/0.079/28.24	28.73/0.775/0.144/65.96	34.05/0.933/0.033/23.75	31.20/0.883/0.072/43.51	27.85/0.788/0.162/84.22
RCOT [38]	34.92/0.928/0.059/18.95	32.68/0.885/0.083/24.33	29.53/0.808/0.132/48.54	34.19/0.935/0.046/26.51	31.65/0.896/0.075/48.24	28.31/0.808/0.160/80.86
DA-RCOT	35.02/0.929/0.048/13.15	32.75/0.885/0.072/18.15	29.65/0.810/0.121/40.75	34.29/0.939/0.036/16.15	31.70/0.898/0.060/38.87	28.59/0.816/0.145/72.27

Fig. 6. Visual comparison of task-specific results of a real hazy from O-HAZE, a real rainy image from SPANet, and a noisy image from BSD68 with $\sigma = 50$. DA-RCOT restores sharp images with more faithful structural contents (colors and textures). Please zoom in for better visualization.

and colors). These results further underscore its expressive power for addressing single degradations in comparison to other all-in-one models and general restorers.

5.3 Robustness to the Number of Degradation Types

The robustness to degradation number is an important property of All-in-One models. Specifically, how well can these models adapt as the number of degradations increases? To explore this capability, we establish a task queue: 1) deraining, 2) denoising with $\sigma = 25$, 3) dehazing, 4) deblurring, and 5) low-light enhancement. The tasks are added sequentially for all-in-one training and we record

the deraining performance on Rain100L as the degradation number increases. The dataset settings follow those of the five-degradation All-in-One evaluation.

Compared Methods. Four methods are selected for comparisons, including general restorers Restormer [19], IR-SDE [22] and All-in-One PromptIR [32] and DA-CLIP [33].

Figure 7 displays the quantitative results of deraining against the number of degradation types. We can observe from the figure that as compared to the general restorers [18], [19], the All-in-One models are generally more robust as the number of degradations increases. Notably, DA-RCOT achieves the highest quantitative performance and

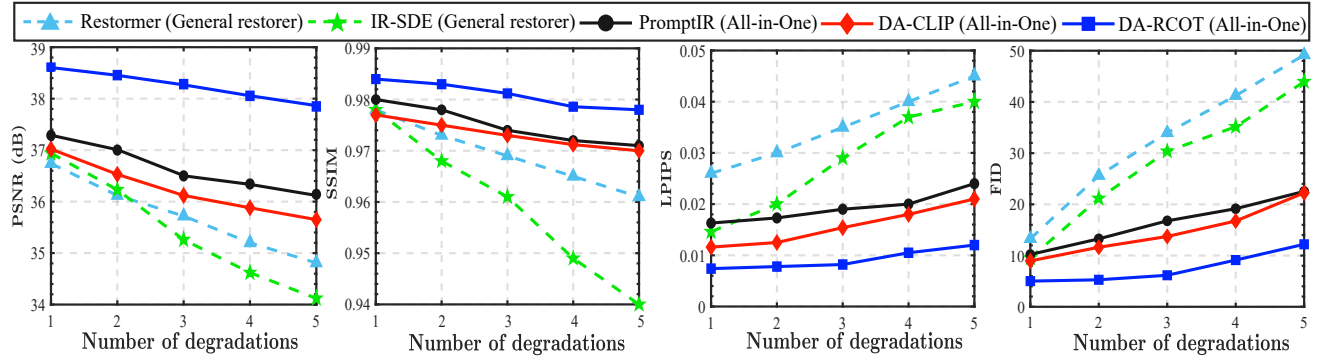


Fig. 7. Numerical comparison of robustness to the number of degradation types. As the degradation number increases, DA-RCOT delivers pleasant robustness while achieving the best quantitative performance on the deraining task in comparison with other methods.

exhibits the least decline as the number of degradations goes up, which demonstrates its better robustness as compared to other methods. The underlying reason should be that the residual embeddings of DA-RCOT encode more intrinsic degradation semantics, dynamically adapting the OT map to handle heterogeneous degradations.

5.4 Generalization to Unseen Degradation Levels

TABLE 4

The OOD deraining results on Rain100L (light rain images), where the models are trained on Rain100H (heavy rain images).

Method	PSNR (\uparrow)	SSIM (\uparrow)	LPIPS (\downarrow)	FID (\downarrow)
Restormer [19]	29.85	0.921	0.121	53.54
IR-SDE [22]	29.53	0.912	0.092	33.65
AirNet [29]	30.02	0.933	0.110	46.19
PromptIR [32]	31.65	0.929	0.076	43.41
DA-CLIP [33]	33.61	0.950	0.056	34.11
RCOT [38]	32.85	0.945	0.048	32.63
DA-RCOT	34.23	0.962	0.032	16.77

TABLE 5

The OOD denoising results on BSD68 with unseen noise levels $\sigma = 60$ and $\sigma = 75$, where the models are trained on noisy images from BSD400 [76] and WED [77] with noise levels $\sigma \in \{15, 25, 50\}$.

Method	$\sigma = 60$		$\sigma = 75$	
	Blur + Noise	DA-CLIP	PromptIR	DA-RCOT
Restormer [19]	19.23/0.481/0.242/117.7	15.56/0.398/0.423/165.6		
IR-SDE [22]	17.84/0.413/0.236/122.0	15.10/0.337/0.375/148.3		
AirNet [29]	19.25/0.483/0.249/118.6	15.87/0.406/0.392/164.6		
PromptIR [32]	23.78/0.616/0.223/101.2	19.23/0.502/0.389/152.3		
DA-CLIP [33]	20.18/0.495/0.198/93.15	16.78/0.384/0.342/133.2		
RCOT [38]	<u>25.12/0.656/0.184/88.13</u>	<u>19.85/0.515/0.326/121.5</u>		
DA-RCOT	<u>25.89/0.685/0.167/66.95</u>	<u>21.64/0.571/0.276/108.6</u>		

As observed in Figure 4, the residual embeddings of different noise levels are clustered together, exhibiting level-specific positional relationships. To validate the advantages of these characteristics, we evaluate DA-RCOT on out-of-distribution (OOD) data with unseen degradation levels, where the model was trained on data with other levels of the same degradation. Specifically, we conduct two experiments. In the first evaluation, the DA-RCOT map is trained on Rain100H [39] (heavily rainy images) and tested on Rain100L [39] (lightly rainy images). In the second evaluation, we test the performance of the DA-RCOT map on severe noise levels $\sigma = 60$ and $\sigma = 75$, where the model

is trained on the mixed noisy images from BSD400 [76] and WED [77] datasets with noise levels $\sigma \in \{15, 25, 50\}$.

Tables 4 and 5 present the deraining and denoising quantitative results on OOD degradation levels. We can observe that All-in-One models generally perform better than regular general restorers. DA-RCOT exhibits superior generalization ability to unseen degradation levels as compared to other methods, highlighting the advantages of the residual embedding in capturing the intrinsic degradation semantics beyond levels, which coincides with the unique cluster patterns observed in Figure 4. Different from RCOT, DA-RCOT disentangles multi-scale embeddings and conditions them at different scales within the transport map network. This approach imparts richer correlations between levels and more intrinsic degradation semantics, thereby enhancing the OT map's generalization ability across degradation levels.

5.5 Real-world Images with Multiple Degradations

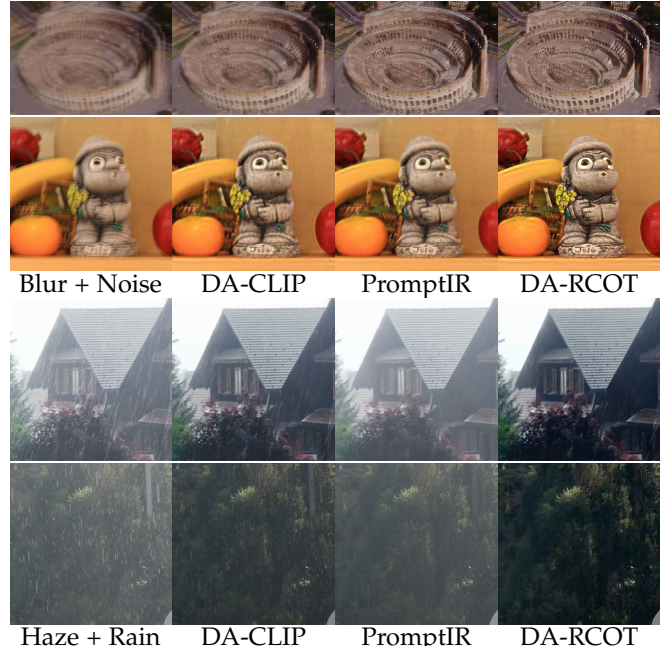


Fig. 8. Visual comparisons of All-in-One models addressing multiple degradations. The first two rows display the results for blurry and noisy images, while the last two rows display those for hazy and rainy images.

The images captured from the real world are sometimes corrupted by multiple degradations due to adverse weather

TABLE 6

The qualitative results of the model with different conditions for the second pass restoration. Metrics are reported in the form of PSNR(\uparrow)/LPIPS(\downarrow).

Method	SOTS	Rain100L	BSD68 $_{\sigma=25}$	GoPro	LOL	Average
w/o any condition	27.56/0.054	35.37/0.038	31.10/0.105	27.32/0.177	20.60/0.135	28.39/0.102
conditioned on \hat{x}_0	27.87/0.052	35.82/0.039	30.43/0.115	27.41/0.172	20.73/0.122	28.45/0.100
conditioned on \mathbf{R}_0	30.26/0.016	36.88/0.024	31.05/0.099	28.12/0.155	22.76/0.097	29.81/0.078
conditioned on $\{\mathbf{R}_i\}_{i=1,2,3}$	30.96/0.008	37.87/0.012	31.22/0.082	28.68/0.135	23.25/0.084	30.40/0.064

conditions and the property of imaging devices. In this sense, a practical challenge for the All-in-One models is to handle these multiple degradations. Here, we compare DA-RCOT with PromptIR [32] and DA-CLIP [33] to explore their capability in handling such complex scenarios. We consider two common real-world scenarios with degraded images that contain 1) blur and noise or 2) haze and rain. For the noise and blur case, we combine the noisy images from BSD400 [76] and WED [77] and blurry images from GoPro [42] for co-training. For the haze and rain case, we train models combining hazy images from SOTS [80] and rainy images from SPANet [79]. For the evaluation, we collect 49 real images of haze and rain or blur and noise. The images and restored results are in the supplementary materials.

TABLE 7

Quantitative comparison of the quality assessment of the 49 Real multiple-degradation images with average NIQE(\downarrow)/PIQE(\downarrow) metrics.

Method	Blur and Noise	Rain and Haze
Restormer [19]	8.06/92.54	8.96/118.8
IR-SDE [22]	8.14/97.20	7.87/102.1
AirNet [29]	8.23/102.4	8.85/113.2
PromptIR [32]	5.01/68.59	6.28/92.79
DA-CLIP [33]	7.87/82.84	7.09/105.7
RCOT [38]	4.82/60.23	6.33/89.64
DA-RCOT	3.75/46.27	4.62/57.40

Table 7 reports the non-reference quantitative results on 49 real multi-degradation images, which validates the effectiveness of DA-RCOT in handling real-world multiple degradations in a single image. The visual examples are illustrated in Figure 8. For the noise and blur cases, DA-CLIP [33] restores images with remaining blur and noise and arouses significant artifacts around the edges. PromptIR [32] produces results with over-smoothed structures. For the haze and rain cases, DA-CLIP removes the haze and rain inadequately while PromptIR performs better at removing the rain but fails to address the haze. In comparison, DA-RCOT effectively removes the noise and blur or haze and rain, producing sharp images with well-preserved structural contents. These results demonstrate the adaptability of our DA-RCOT in addressing multiple real-world degradations. The advantages can be credited to the optimal restoration learning between multi-domain distributions, along with the conditioning of residual embeddings, which enables the OT map to adaptively adjust its behaviors for structure-preserving and degradation-aware restoration.

5.6 Ablation Studies

5.6.1 Effect of residual embeddings conditioning (REC)

We first justify the importance of the two-pass residual embeddings conditioning (REC) mechanism, i.e., utilizing

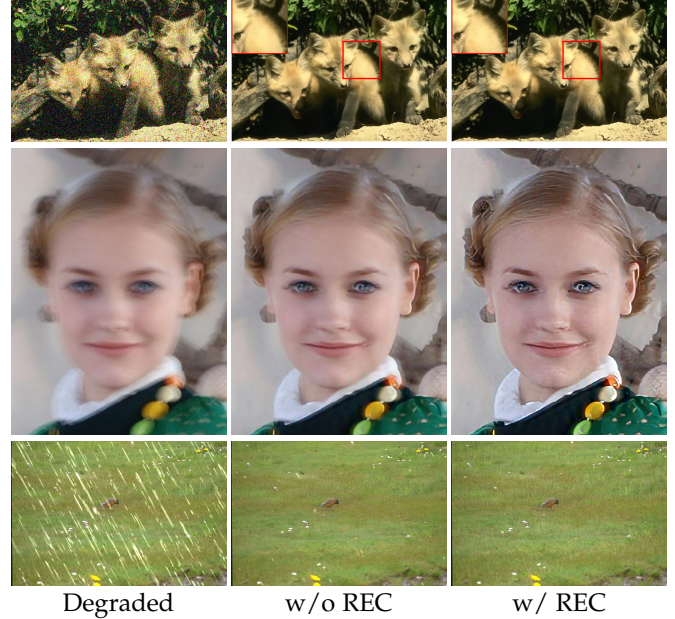


Fig. 9. Visual results to show the importance of REC. The model with REC produces sharper images with better structural contents.

the multi-scale residual embeddings $\{\mathbf{R}_i\}_{i=1,2,3}$ as conditions for the OT map. We try different conditions for the OT map: a) w/o any condition, b) intermediate restored result \hat{x}_0 , c) original residual embedding \mathbf{R}_0 (RCOT), and d) multi-scale residual embeddings $\{\mathbf{R}_i\}_{i=1,2,3}$ (DA-RCOT).

TABLE 8

Effect of using different losses. We report the average metrics of models using different losses for the three-degradation configuration.

	Loss	PSNR \uparrow	SSIM \uparrow	LPIPS \downarrow	FID \downarrow
Unpaired	\mathcal{L}_u	29.28	0.855	0.106	67.13
	$\mathcal{L}_u + \mathcal{L}_{task}$	30.20	0.897	0.086	53.24
Paired	L_1 distance	31.82	0.911	0.087	53.21
	\mathcal{L}_p	32.35	0.915	0.063	37.12
	$\mathcal{L}_p + \mathcal{L}_{task}$	32.60	0.917	0.055	30.06

Table 6 presents the All-in-One results on five degradation configurations. We can observe that the two-pass residual embedding conditioning mechanism provides a notable improvement as compared to the methods conditioned or nothing or \hat{x}_0 , demonstrating that the residual embeddings capture valuable degradation semantics for AIR. As compared to the original \mathbf{R}_0 , multi-scale residual embeddings $\{\mathbf{R}_i\}_{i=1,2,3}$ encode and decouple more intrinsic degradation knowledge and structural information, adapting the OT map for degradation-aware restoration. Figure 9 provides visual examples of denoising, deblurring, and deraining with no conditioning (w/o REC) and with $\{\mathbf{R}_i\}_{i=1,2,3}$ as

TABLE 9
Results using transport costs with $g(\hat{r})$ (FROT) and without $g(\hat{r})$. Metrics are reported in the form of PSNR(\uparrow)/LPIPS(\downarrow).

Method	SOTS	Rain100L	BSD68 $_{\sigma=25}$	GoPro	LOL	Average
w/o $g(\hat{r})$	30.84/0.019	37.28/0.018	31.02/0.096	28.24/0.158	22.87/0.103	30.05/0.079
w/ $g(\hat{r})$	31.26/0.007	38.22/0.008	31.22/0.080	28.86/0.135	23.25/0.084	30.40/0.064

conditions (w/ REC). The results show that the model without REC removes the degradations inadequately and causes loss of details, while the one with REC can restore sharp images with better structural details.

5.6.2 Effect of using different losses

We further explore the effect of using different losses to validate the effectiveness of FROT objectives (Eq. 10 and 11) for modeling AIR and the \mathcal{L}_{task} (Eq. 16) for enhancing the task semantic features of dense residual embedding \mathbf{R}_1 . Table 8 reports the quantitative All-in-One results under the three-degradation configuration. The results show that in both unpaired and paired settings, incorporating \mathcal{L}_{task} to emphasize the task semantics brings a significant improvement, particularly to the unpaired case. On the other hand, the FROT objective \mathcal{L}_p outperforms the L_1 distance for supervised learning, with an average improvement of 0.53 dB in PSNR and a reduction of 0.024 in LPIPS. Notably, the perceptual quality metrics (LPIPS and FID) of $\mathcal{L}_u + \mathcal{L}_{task}$ for unpaired learning evenly match those of the L_1 distance case for paired learning. These results substantiate the advantage of modeling AIR from an optimal transport perspective with residual guidance.

5.6.3 Effect of the residual regularization in FROT objective

We investigate the effect of the residual regularization in the FROT objective. In Table 9, we compare the performance of the models trained under the FROT cost (w/ $g(\hat{r})$) and OT cost (w/o $g(\hat{r})$). The results show that residual regularization, which integrates degradation-specific knowledge into transport costs, brings meaningful gains.

5.7 Discussion and Analysis

5.7.1 Parameter quantity and computational complexity

We compare the parameter quantity and computational complexity in Table 10. We compare with the most recent methods IR-SDE [22], PromptIR [32], and DA-CLIP [33]. Table 10 along with previous results shows that our DA-RCOT achieves significantly superior performance while incurring a slight increase in computational cost. The inference time and parameter efficiency of DA-RCOT are superior compared to the state-of-the-art method DA-CLIP [33].

TABLE 10

Comparison of the number of parameters, model computational efficiency, and inference time. The flops and inference time are computed on deraining images of size 256×256.

Method	IR-SDE	PromptIR	DA-CLIP	DA-RCOT
#Param	36.2M	36.3M	174.1M	49.8M
Flops	117G	158G	118.5G	218G
Inference time	4.23s	0.15s	4.59s	0.22s

TABLE 11
The influence of the multi-scale REC being integrated into different network backbones. The metrics are presented as PSNR (\uparrow)/SSIM (\uparrow)/LPIPS (\downarrow)/FID (\downarrow) values.

Method	MPRNet [18]	NAFNet [84]	Restormer [19]
w/o REC	34.95/0.964/0.039/21.61	35.58/0.969/0.036/18.35	36.74/0.978/0.023/13.29
w/ REC	36.78/0.972/0.022/12.58	37.10/0.976/0.017/11.86	38.22/0.984/0.014/7.013

5.7.2 Generalization of REC beyond network designs

The two-pass multi-scale REC mechanism forms a plugin module (Figure 2), allowing us to use any architecture as a base model to generate the restored result, and then use this result to calculate the residual for the second-pass restoration. We have now included a comparison on Rain100L dataset [28] between the MPRNet [18], NAFNet [84], Restormer [19] methods and the corresponding methods with the proposed REC mechanism. The results in Table 11 show that the REC mechanism brings meaningful boosts to three benchmark network architectures, which validates its versatility and generalizability beyond network designs.

5.7.3 Training Cost Curves

In Figure 10, we provide the cost curves over All-in-One three degradations and task-specific deraining and denoising of the transport map T_θ and the potential φ_w in the training process. The T_θ cost curve is normalized to [0, 1]. φ_w cost is scaled to [0, 1] and then take the negative. We can observe that the curves of the transport map and the potential converge well in an adversarial manner.

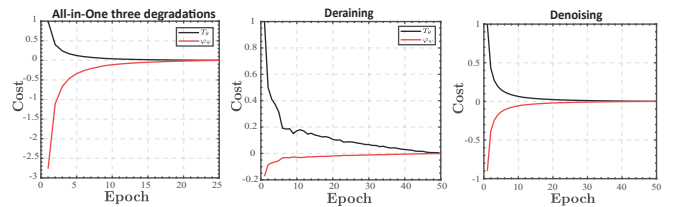


Fig. 10. The cost curves for three tasks. The cost of T_θ is scaled to [0, 1]. The cost of φ_w is scaled to [0, 1] and then takes the negative.

5.8 CONCLUSION, LIMITATION AND FUTURE WORK

This paper has proposed a Degradation-Aware Residual-Conditioned Optimal Transport (DA-RCOT) approach for the AIR problem, which models AIR as an OT problem and introduces the novel transport residual as a degradation-specific cue for both transport cost and transport map. We condition the transport map on the decoupled multi-scale residual embeddings via a two-pass process. This process injects the intrinsic degradation knowledge and structural information from multi-scale residual embedding into the OT map, which can thereby adaptively adjust its behaviors for

structure-preserving all-in-one restoration. Extensive experiments demonstrate that DA-RCOT achieves state-of-the-art performance on a range of image restoration tasks under all-in-one and task-specific configurations. Particularly, DA-RCOT delivers superior adaptability to real-world scenarios even with multiple degradations and unique robustness to both degradation levels and the number of degradations.

We acknowledge that there are some potential limitations. For example, when the noise level is much too severe, the generalization performance of DA-RCOT can deteriorate to some extent since the severe noise as a condition may interrupt the original features. In the future, we are interested in adapting the OT model for multi-modality one-to-many generation and translation problems.

REFERENCES

- [1] K. He, J. Sun, and X. Tang, "Single image haze removal using dark channel prior," *IEEE Transactions on Pattern Analysis and Machine Intelligence (TPAMI)*, vol. 33, no. 12, pp. 2341–2353, 2010.
- [2] J. Pan, D. Sun, H. Pfister, and M.-H. Yang, "Blind image deblurring using dark channel prior," in *Proceedings of the IEEE/CVF Conference on Computer Vision and Pattern Recognition (CVPR)*, pp. 1628–1636, 2016.
- [3] D. Ulyanov, A. Vedaldi, and V. Lempitsky, "Deep image prior," in *Proceedings of the IEEE/CVF Conference on Computer Vision and Pattern Recognition (CVPR)*, pp. 9446–9454, 2018.
- [4] Z. Xu and J. Sun, "Image inpainting by patch propagation using patch sparsity," *IEEE Transactions on Image Processing (TIP)*, vol. 19, no. 5, pp. 1153–1165, 2010.
- [5] J.-L. Wang, T.-Z. Huang, X.-L. Zhao, T.-X. Jiang, and M. K. Ng, "Multi-dimensional visual data completion via low-rank tensor representation under coupled transform," *IEEE Transactions on Image Processing (TIP)*, vol. 30, pp. 3581–3596, 2021.
- [6] R. Fergus, B. Singh, A. Hertzmann, S. T. Roweis, and W. T. Freeman, "Removing camera shake from a single photograph," in *Acm Siggraph 2006 Papers*, pp. 787–794, 2006.
- [7] J. Sun, Z. Xu, and H.-Y. Shum, "Image super-resolution using gradient profile prior," in *Proceedings of the IEEE/CVF Conference on Computer Vision and Pattern Recognition (CVPR)*, pp. 1–8, IEEE, 2008.
- [8] Q. Shan, J. Jia, and A. Agarwala, "High-quality motion deblurring from a single image," *Acm transactions on graphics (TOG)*, vol. 27, no. 3, pp. 1–10, 2008.
- [9] H. Ji and K. Wang, "Robust image deblurring with an inaccurate blur kernel," *IEEE Transactions on Image Processing (TIP)*, vol. 21, no. 4, pp. 1624–1634, 2011.
- [10] X. Tang, X. Zhao, J. Liu, J. Wang, Y. Miao, and T. Zeng, "Uncertainty-aware unsupervised image deblurring with deep residual prior," in *Proceedings of the IEEE/CVF Conference on Computer Vision and Pattern Recognition (CVPR)*, pp. 9883–9892, June 2023.
- [11] K. He, X. Zhang, S. Ren, and J. Sun, "Deep residual learning for image recognition," in *Proceedings of the IEEE/CVF Conference on Computer Vision and Pattern Recognition (CVPR)*, pp. 770–778, 2016.
- [12] A. Vaswani, N. Shazeer, N. Parmar, J. Uszkoreit, L. Jones, A. N. Gomez, Ł. Kaiser, and I. Polosukhin, "Attention is all you need," *Advances in Neural Information Processing Systems (NeurIPS)*, vol. 30, 2017.
- [13] A. Dosovitskiy, L. Beyer, A. Kolesnikov, D. Weissenborn, X. Zhai, T. Unterthiner, M. Dehghani, M. Minderer, G. Heigold, S. Gelly, J. Uszkoreit, and N. Houlsby, "An image is worth 16x16 words: Transformers for image recognition at scale," in *International Conference on Learning Representations (ICLR)*, 2021.
- [14] Z. Liu, Y. Lin, Y. Cao, H. Hu, Y. Wei, Z. Zhang, S. Lin, and B. Guo, "Swin transformer: Hierarchical vision transformer using shifted windows," in *Proceedings of the IEEE/CVF Conference on Computer Vision and Pattern Recognition (CVPR)*, pp. 10012–10022, 2021.
- [15] W.-S. Lai, J.-B. Huang, N. Ahuja, and M.-H. Yang, "Deep laplacian pyramid networks for fast and accurate super-resolution," in *Proceedings of the IEEE Conference on Computer Vision and Pattern Recognition (CVPR)*, pp. 624–632, 2017.
- [16] W.-S. Lai, J.-B. Huang, N. Ahuja, and M.-H. Yang, "Fast and accurate image super-resolution with deep laplacian pyramid networks," *IEEE Transactions on Pattern Analysis and Machine Intelligence (TPAMI)*, vol. 41, no. 11, pp. 2599–2613, 2018.
- [17] K. Zhang, W. Zuo, and L. Zhang, "Ffdnet: Toward a fast and flexible solution for cnn-based image denoising," *IEEE Transactions on Image Processing (TIP)*, vol. 27, no. 9, pp. 4608–4622, 2018.
- [18] S. W. Zamir, A. Arora, S. Khan, M. Hayat, F. S. Khan, M.-H. Yang, and L. Shao, "Multi-stage progressive image restoration," in *Proceedings of the IEEE/CVF Conference on Computer Vision and Pattern Recognition (CVPR)*, 2021.
- [19] S. W. Zamir, A. Arora, S. Khan, M. Hayat, F. S. Khan, and M.-H. Yang, "Restormer: Efficient transformer for high-resolution image restoration," in *Proceedings of the IEEE/CVF Conference on Computer Vision and Pattern Recognition (CVPR)*, 2022.
- [20] J. Liang, J. Cao, G. Sun, K. Zhang, L. Van Gool, and R. Timofte, "Swinir: Image restoration using swin transformer," in *Proceedings of the IEEE/CVF International Conference on Computer Vision (ICCV)*, pp. 1833–1844, 2021.
- [21] L. Chen, X. Chu, X. Zhang, and J. Sun, "Simple baselines for image restoration," in *European Conference on Computer Vision (ECCV)*, pp. 17–33, 2022.
- [22] Z. Luo, F. K. Gustafsson, Z. Zhao, J. Sjölund, and T. B. Schön, "Image restoration with mean-reverting stochastic differential equations," in *International Conference on Machine Learning (ICML)*, pp. 23045–23066, PMLR, 2023.
- [23] M. Zhou, J. Huang, C.-L. Guo, and C. Li, "Fourmer: an efficient global modeling paradigm for image restoration," in *International Conference on Machine Learning (ICML)*, 2023.
- [24] J. Levinson, J. Askeland, J. Becker, J. Dolson, D. Held, S. Kammel, J. Z. Kolter, D. Langer, O. Pink, V. Pratt, et al., "Towards fully autonomous driving: Systems and algorithms," in *2011 IEEE Intelligent Vehicles Symposium (IV)*, pp. 163–168, IEEE, 2011.
- [25] A. Prakash, K. Chitta, and A. Geiger, "Multi-modal fusion transformer for end-to-end autonomous driving," in *Proceedings of the IEEE/CVF Conference on Computer Vision and Pattern Recognition (CVPR)*, pp. 7077–7087, 2021.
- [26] M. Liang, B. Yang, S. Wang, and R. Urtasun, "Deep continuous fusion for multi-sensor 3d object detection," in *Proceedings of the European conference on computer vision (ECCV)*, pp. 641–656, 2018.
- [27] G. Petschnigg, R. Szeliski, M. Agrawala, M. Cohen, H. Hoppe, and K. Toyama, "Digital photography with flash and no-flash image pairs," *ACM transactions on graphics (TOG)*, vol. 23, no. 3, pp. 664–672, 2004.
- [28] Q. Fan, D. Chen, L. Yuan, G. Hua, N. Yu, and B. Chen, "A general decoupled learning framework for parameterized image operators," *IEEE Transactions on Pattern Analysis and Machine Intelligence (TPAMI)*, vol. 43, no. 1, pp. 33–47, 2019.
- [29] B. Li, X. Liu, P. Hu, Z. Wu, J. Lv, and X. Peng, "All-in-one image restoration for unknown corruption," in *Proceedings of the IEEE/CVF conference on computer vision and pattern recognition*, pp. 17452–17462, 2022.
- [30] J. M. J. Valanarasu, R. Yasarla, and V. M. Patel, "Transweather: Transformer-based restoration of images degraded by adverse weather conditions," in *Proceedings of the IEEE/CVF Conference on Computer Vision and Pattern Recognition (CVPR)*, pp. 2353–2363, 2022.
- [31] J. Zhang, J. Huang, M. Yao, Z. Yang, H. Yu, M. Zhou, and F. Zhao, "Ingredient-oriented multi-degradation learning for image restoration," in *Proceedings of the IEEE/CVF Conference on Computer Vision and Pattern Recognition (CVPR)*, pp. 5825–5835, 2023.
- [32] V. Potlapalli, S. W. Zamir, S. Khan, and F. S. Khan, "Promptir: Prompting for all-in-one blind image restoration," *Advances in Neural Information Processing Systems (NeurIPS)*, 2023.
- [33] Z. Luo, F. K. Gustafsson, Z. Zhao, J. Sjölund, and T. B. Schön, "Controlling vision-language models for multi-task image restoration," in *The Twelfth International Conference on Learning Representations (ICLR)*, 2024.
- [34] E. Zamfir, Z. Wu, N. Mehta, D. D. Paudel, Y. Zhang, and R. Timofte, "Efficient degradation-aware any image restoration," *arXiv preprint arXiv:2405.15475*, 2024.
- [35] Y. Blau and T. Michaeli, "The perception-distortion tradeoff," in *Proceedings of the IEEE/CVF Conference on Computer Vision and Pattern Recognition (CVPR)*, pp. 6228–6237, 2018.
- [36] G. Ohayon, T. J. Adrai, M. Elad, and T. Michaeli, "Reasons for the superiority of stochastic estimators over deterministic ones:

Robustness, consistency and perceptual quality," in *International Conference on Machine Learning (ICML)*, pp. 26474–26494, 2023.

[37] T. J. Adrai, G. Ohayon, M. Elad, and T. Michaeli, "Deep optimal transport: A practical algorithm for photo-realistic image restoration," in *Advances in Neural Information Processing Systems (NeurIPS)*, 2023.

[38] X. Tang, X. Hu, X. Gu, and J. Sun, "Residual-conditioned optimal transport: Towards structure-preserving unpaired and paired image restoration," in *International Conference on Machine Learning (ICML)*, pp. 47757–47777, PMLR, 2024.

[39] W. Yang, R. T. Tan, J. Feng, J. Liu, Z. Guo, and S. Yan, "Deep joint rain detection and removal from a single image," in *Proceedings of the IEEE/CVF Conference on Computer Vision and Pattern Recognition (CVPR)*, pp. 1357–1366, 2017.

[40] D. Martin, C. Fowlkes, D. Tal, and J. Malik, "A database of human segmented natural images and its application to evaluating segmentation algorithms and measuring ecological statistics," in *Proceedings of the IEEE/CVF Conference on Computer Vision and Pattern Recognition (CVPR)*, vol. 2, pp. 416–423, 2001.

[41] B. Li, W. Ren, D. Fu, D. Tao, D. Feng, W. Zeng, and Z. Wang, "Benchmarking single-image dehazing and beyond," *IEEE Transactions on Image Processing (TIP)*, vol. 28, no. 1, pp. 492–505, 2018.

[42] S. Nah, T. Hyun Kim, and K. Mu Lee, "Deep multi-scale convolutional neural network for dynamic scene deblurring," in *Proceedings of the IEEE conference on computer vision and pattern recognition*, pp. 3883–3891, 2017.

[43] C. Wei, W. Wang, W. Yang, and J. Liu, "Deep retinex decomposition for low-light enhancement," *arXiv preprint arXiv:1808.04560*, 2018.

[44] D. Ren, W. Zuo, Q. Hu, P. Zhu, and D. Meng, "Progressive image deraining networks: A better and simpler baseline," in *Proceedings of the IEEE/CVF conference on computer vision and pattern recognition*, pp. 3937–3946, 2019.

[45] C. Wang, J. Pan, W. Wang, J. Dong, M. Wang, Y. Ju, and J. Chen, "Promptrestorer: A prompting image restoration method with degradation perception," in *Advances in Neural Information Processing Systems (NeurIPS)*, 2023.

[46] X. Chen, H. Li, M. Li, and J. Pan, "Learning a sparse transformer network for effective image deraining," in *Proceedings of the IEEE/CVF Conference on Computer Vision and Pattern Recognition (CVPR)*, pp. 5896–5905, 2023.

[47] K. Zhang, W. Zuo, and L. Zhang, "Learning a single convolutional super-resolution network for multiple degradations," in *Proceedings of the IEEE conference on computer vision and pattern recognition*, pp. 3262–3271, 2018.

[48] R. Li, J. Pan, Z. Li, and J. Tang, "Single image dehazing via conditional generative adversarial network," in *Proceedings of the IEEE/CVF Conference on Computer Vision and Pattern Recognition (CVPR)*, pp. 8202–8211, 2018.

[49] J. Pan, J. Dong, Y. Liu, J. Zhang, J. Ren, J. Tang, Y.-W. Tai, and M.-H. Yang, "Physics-based generative adversarial models for image restoration and beyond," *IEEE Transactions on Pattern Analysis and Machine Intelligence (TPAMI)*, vol. 43, no. 7, pp. 2449–2462, 2020.

[50] G. G. Chrysos, J. Kossaifi, and S. Zafeiriou, "Rocgan: Robust conditional gan," *International Journal of Computer Vision (IJCV)*, vol. 128, pp. 2665–2683, 2020.

[51] M. Mirza and S. Osindero, "Conditional generative adversarial nets," *arXiv preprint arXiv:1411.1784*, 2014.

[52] A. Bora, E. Price, and A. G. Dimakis, "Ambientgan: Generative models from lossy measurements," in *International Conference on Machine Learning (ICML)*, 2018.

[53] C. Saharia, J. Ho, W. Chan, T. Salimans, D. J. Fleet, and M. Norouzi, "Image super-resolution via iterative refinement," *IEEE Transactions on Pattern Analysis and Machine Intelligence (TPAMI)*, vol. 45, no. 4, pp. 4713–4726, 2022.

[54] B. Kawar, G. Vaksman, and M. Elad, "Snips: Solving noisy inverse problems stochastically," *Advances in Neural Information Processing Systems (NeurIPS)*, vol. 34, pp. 21757–21769, 2021.

[55] B. Kawar, M. Elad, S. Ermon, and J. Song, "Denoising diffusion restoration models," in *Advances in Neural Information Processing Systems (NeurIPS)*, 2022.

[56] H. Chung, J. Kim, M. T. Mccann, M. L. Klasky, and J. C. Ye, "Diffusion posterior sampling for general noisy inverse problems," in *International Conference on Learning Representations (ICLR)*, 2023.

[57] S. Gao, X. Liu, B. Zeng, S. Xu, Y. Li, X. Luo, J. Liu, X. Zhen, and B. Zhang, "Implicit diffusion models for continuous super-resolution," in *Proceedings of the IEEE/CVF Conference on Computer Vision and Pattern Recognition (CVPR)*, pp. 10021–10030, 2023.

[58] G. Monge, "Mémoire sur la théorie des déblais et des remblais," *Mem. Math. Phys. Acad. Royale Sci.*, pp. 666–704, 1781.

[59] L. V. Kantorovich, "On the translocation of masses," in *Dokl. Akad. Nauk. USSR (NS)*, vol. 37, pp. 199–201, 1942.

[60] M. Arjovsky, S. Chintala, and L. Bottou, "Wasserstein generative adversarial networks," in *International Conference on Machine Learning (ICML)*, pp. 214–223, PMLR, 2017.

[61] I. Gulrajani, F. Ahmed, M. Arjovsky, V. Dumoulin, and A. C. Courville, "Improved training of wasserstein gans," *Advances in Neural Information Processing Systems (NeurIPS)*, vol. 30, 2017.

[62] X. Gu, L. Yang, J. Sun, and Z. Xu, "Optimal transport-guided conditional score-based diffusion model," in *Advances in Neural Information Processing Systems (NeurIPS)*, 2023.

[63] A. Korotin, D. Selikhanovych, and E. Burnaev, "Neural optimal transport," in *International Conference on Learning Representations (ICLR)*, 2023.

[64] A. Korotin, D. Selikhanovych, and E. Burnaev, "Kernel neural optimal transport," in *International Conference on Learning Representations (ICLR)*, 2023.

[65] W. Wang, F. Wen, Z. Yan, and P. Liu, "Optimal transport for unsupervised denoising learning," *IEEE Transactions on Pattern Analysis and Machine Intelligence (TPAMI)*, vol. 45, no. 2, pp. 2104–2118, 2022.

[66] C. Villani *et al.*, *Optimal transport: old and new*, vol. 338. Springer, 2009.

[67] R. Rockafellar, "Integral functionals, normal integrands and measurable selections," *Nonlinear Operators and the Calculus of Variations*, pp. 157–207, 1976.

[68] A. Pratelli, "On the equality between monge's infimum and kantorovich's minimum in optimal mass transportation," *Annales de l'Institut Henri Poincaré (B) Probability and Statistics*, vol. 43, no. 1, pp. 1–13, 2007.

[69] A. Voynov, Q. Chu, D. Cohen-Or, and K. Aberman, "p+: Extended textual conditioning in text-to-image generation," *arXiv preprint arXiv:2303.09522*, 2023.

[70] J.-Y. Zhu, T. Park, P. Isola, and A. A. Efros, "Unpaired image-to-image translation using cycle-consistent adversarial networks," in *Proceedings of the IEEE International Conference on Computer Vision (ICCV)*, pp. 2223–2232, 2017.

[71] R. Zhang, P. Isola, A. A. Efros, E. Shechtman, and O. Wang, "The unreasonable effectiveness of deep features as a perceptual metric," in *Proceedings of the IEEE/CVF Conference on Computer Vision and Pattern Recognition (CVPR)*, pp. 586–595, 2018.

[72] M. Heusel, H. Ramsauer, T. Unterthiner, B. Nessler, and S. Hochreiter, "Gans trained by a two time-scale update rule converge to a local nash equilibrium," *Advances in Neural Information Processing Systems (NeurIPS)*, vol. 30, 2017.

[73] A. Mittal, R. Soundararajan, and A. C. Bovik, "Making a "completely blind" image quality analyzer," *IEEE Signal processing letters*, vol. 20, no. 3, pp. 209–212, 2012.

[74] N. Venkatanath, D. Praneeth, M. C. Bh, S. S. Channappayya, and S. S. Medasani, "Blind image quality evaluation using perception based features," in *2015 twenty first national conference on communications (NCC)*, pp. 1–6, IEEE, 2015.

[75] C. Ledig, L. Theis, F. Huszár, J. Caballero, A. Cunningham, A. Acosta, A. Aitken, A. Tejani, J. Totz, Z. Wang, *et al.*, "Photo-realistic single image super-resolution using a generative adversarial network," in *Proceedings of the IEEE/CVF International Conference on Computer Vision (ICCV)*, pp. 4681–4690, 2017.

[76] P. Arbelaez, M. Maire, C. Fowlkes, and J. Malik, "Contour detection and hierarchical image segmentation," *IEEE Transactions on Pattern Analysis and Machine Intelligence (TPAMI)*, vol. 33, no. 5, pp. 898–916, 2010.

[77] K. Ma, Z. Duanmu, Q. Wu, Z. Wang, H. Yong, H. Li, and L. Zhang, "Waterloo exploration database: New challenges for image quality assessment models," *IEEE Transactions on Image Processing (TIP)*, vol. 26, no. 2, pp. 1004–1016, 2016.

[78] R. Franzen, "Kodak lossless true color image suite," *source: http://r0k.us/graphics/kodak*, vol. 4, no. 2, p. 9, 1999.

[79] T. Wang, X. Yang, K. Xu, S. Chen, Q. Zhang, and R. W. Lau, "Spatial attentive single-image deraining with a high quality real rain dataset," in *Proceedings of the IEEE/CVF Conference on Computer Vision and Pattern Recognition (CVPR)*, June 2019.

[80] C. Ancuti, C. Ancuti, R. Timofte, and C. De Vleeschouwer, "O-haze: a dehazing benchmark with real hazy and haze-free outdoor

images," in *Proceedings of the IEEE/CVF Conference on Computer Vision and Pattern Recognition Workshops (CVPRW)*, pp. 754–762, 2018.

[81] Y. Cui, Y. Tao, Z. Bing, W. Ren, X. Gao, X. Cao, K. Huang, and A. Knoll, "Selective frequency network for image restoration," in *The Eleventh International Conference on Learning Representations (ICLR)*, 2023.

[82] Y. Song, Z. He, H. Qian, and X. Du, "Vision transformers for single image dehazing," *IEEE Transactions on Image Processing (TIP)*, vol. 32, pp. 1927–1941, 2023.

[83] Z. Zhang, Y. Jiang, W. Shao, X. Wang, P. Luo, K. Lin, and J. Gu, "Real-time controllable denoising for image and video," in *Proceedings of the IEEE/CVF Conference on Computer Vision and Pattern Recognition (CVPR)*, pp. 14028–14038, June 2023.

[84] X. Chu, L. Chen, and W. Yu, "Nafssr: Stereo image super-resolution using nafnet," in *Proceedings of the IEEE/CVF Conference on Computer Vision and Pattern Recognition Workshops (CVPRW)*, pp. 1239–1248, June 2022.